HDAC3 regulates senescence and lineage-specific transcriptional programs in non-small cell lung cancer

Lillian J. Eichner[1], Stephanie D. Curtis[1], Sonja N. Brun[1], Joshua T. Baumgart[1], Debbie S. Ross[1], Tammy J. Rymoff[1], Reuben J. Shaw[1].

[1]Molecular and Cell Biology Laboratory, The Salk Institute for Biological Studies, La Jolla, CA USA.

*Correspondence: Reuben J. Shaw, Molecular and Cell Biology Laboratory, The Salk Institute for Biological Studies, 10100 N Torrey Pines Road, La Jolla, CA, USA. (858) 453-4100. shaw@salk.edu.

Summary

Transcriptional deregulation is a common feature of many cancers, which is often accompanied by changes in epigenetic controls. These findings have led to the development of therapeutic agents aimed at broad modulation and reprogramming of transcription in a variety of cancers. Histone Deacetylase 3, HDAC3, is one of the main targets of HDAC inhibitors currently in clinical development as cancer therapies, yet the *in vivo* role of HDAC3 in solid tumors is unknown. Here, we define the role of HDAC3 in two genetic engineered models of the most common subtypes of Kras-driven Non-Small Cell Lung Cancer (NSCLC), $Kras^{G12D}$, $STK11^{-/-}$ (KL) and $Kras^{G12D}$, $p53^{-/-}$ (KP), where we found that HDAC3 is strongly required for tumor growth of both genotypes in vivo. Transcriptional profiling and mechanistic studies revealed that HDAC3 represses p65 RelA/NF-kB-mediated induction of the Senescence Associated Secretory Program (SASP). Additionally, HDAC3 was found to cooperate with the lung cancer lineage transcription factor NKX2-1 to mediate expression of a common set of target genes. Leveraging observations about one HDAC3/NKX2-1 common target, FGFR1, we identified that an HDAC3-dependent transcriptional cassette becomes hyperactivated as Kras mutant cancer cells develop resistance to the MEK inhibitor Trametinib, and this can be rescued by treatment with the Class I HDAC inhibitor Entinostat. These unexpected findings reveal new roles for HDAC3 in proliferation control in tumors *in vivo* and identify specific therapeutic contexts for the utilization of HDAC3 inhibitors, whose ability to mechanistically induce SASP may be harnessed therapeutically.

Targeted therapies have begun to prove themselves as successful treatments against cancer types harboring specific, defined vulnerabilities. However, only a small subset of tumor types have targeted therapies currently available, as such agents only exist for a limited number of oncogenic drivers. Moreover, tumors characterized by loss of tumor suppressor genes provide no clear targets against which to develop inhibitors. Transcriptional dependencies of tumors have emerged as definable and therapeutically-tractable liabilities that can be oncogene-agnostic. Much recent effort has focused on targeting epigenetic regulators (e.g. Brd4) as a means to globally affect transcription in such tumors. One case in point are Histone Deacetylase (HDAC) inhibitors, which were originally developed to antagonize the reduced global histone acetylation observed in many tumor types. Clinically well tolerated, several HDAC inhibitors are now FDA

approved to treat blood-borne tumor types. However, efficacy of HDAC inhibitors in solid tumors has been disappointingly limited. One hypothesis to explain this observation is that by targeting multiple HDACs simultaneously, HDAC inhibitors do not achieve the maximal potential benefit of HDAC inhibition as a cancer therapy due to therapeutic window limitations caused by inhibiting too many HDACs simultaneously. And yet, the function of many individual HDACs has yet to be defined in solid tumors *in vivo*.

HDAC3, a Class I HDAC, is unique amongst all HDACs in requiring the Nuclear Receptor Co-Repressor (NCoR) complex for its enzymatic activity. HDAC3 has been shown to deacetylate histone and non-histone proteins, and can function in part through deacetylase-independent mechanisms (1). HDAC3 deletion *in vivo* has identified strikingly tissue specific biological functions and associated transcriptional programs (1), revealing that HDAC3 function is not uniformly through global control of histone acetylation, but is nuanced and directed in a tissue-specific fashion. For example, HDAC3 deletion is brown adipose tissue causes mice to become hypothermic and succumb to acute cold exposure (2), but HDAC3 deletion in the liver induces hypertrophy and metabolic alterations (3-5). Despite clinical advancement of inhibitors of Class I HDACs as therapeutics, any potential role of Class I histone deacetylase HDAC3 in cell proliferation and tumorigenesis remains largely unknown, as its *in vivo* function has mostly been in examined in metabolic tissues.

To assess the role of HDAC3 in solid tumors *in vivo*, we utilized two mouse models engineered to recapitulate the most common subtypes of Kras-mutant Non-Small Cell Lung Cancer (NSCLC); mutant Kras combined with LKB1 loss, $Kras^{LSL\text{-}G12D/+}$ $STK11^{-/-}$ (KL), and mutant Kras combined with p53 loss, $Kras^{LSL\text{-}G12D/+}$ $p53^{-/-}$ (KP). We first examined mice harboring $Kras^{LSL\text{-}G12D/+}$, $STK11^{L/L}$, $ROSA26^{LSL\text{-}luciferase}$, with or without conditional $HDAC3^{L/L}$ (KL-HDAC3). In these mice, intratracheal administration of lentivirus expressing Cre recombinase simultaneously activates $Kras^{G12D}$ and deletes LKB1 (*STK11*) to initiate tumorigenesis in the lung epithelium, and for those bearing $HDAC3^{L/L}$, coincidentally deletes HDAC3. Simultaneous induction of firefly luciferase in infected cells allows for noninvasive longitudinal bioluminescence imaging (BLI) of NSCLC tumor development in the whole animal as we have reported previously (6-9). Tumor growth was markedly reduced in KL-HDAC3 mice compared to KL littermate controls at both early and middle timepoints, exhibiting significantly less tumor area, tumor number and smaller tumor size (Figure 1A-C, S1A-C). Thus, we conclude that HDAC3 supports tumor initiation and tumor growth in the KL model of NSCLC. Employing a similar experimental design, we generated mice harboring $Kras^{LSL\text{-}G12D/+}$, $p53^{L/L}$, $ROSA26^{LSL\text{-}luciferase}$, $HDAC3^{L/L}$ (KP-HDAC3) to test the role of HDAC3 in the KP model of NSCLC. Tumor growth was dramatically reduced in KP-HDAC3 mice compared to KP littermate controls, with significantly less tumor area and smaller tumor size, and a trend toward smaller tumor number (Figure 1D-F, S1D). We conclude that HDAC3 is of critical importance for growth of NSCLC tumors driven by both KL and KP genotypes.

To define the mechanisms underlying the anti-tumor growth phenotypes upon HDAC3 deletion, we deleted HDAC3 in KL and KP tumor cell lines derived from the genetically engineered mouse models (GEMM) using CRISPR-Cas9. Cell lines from KL primary tumors are not readily available due to the fact that, unlike KP tumor cells which lack p53, explanted KL primary tumor cells do not grow in culture, presumed to be from p53 activation-dependent growth arrest. To circumvent this issue, we immortalized explanted KL tumor cells before onset of growth arrest. We plucked individual tumors from KL mice and, after dissociation and collagenase treatment, isolated cells were immortalized with SV40 T-antigen and subsequently purified by Epcam+ cell sorting to generate the epithelial lung tumor cell lines KL LJE1 and KL LJE7 (Figure S2A). These KL cell lines and two established KP cell lines, 634T (10) and KP T3 (6), were infected with lentivirus expressing Cas9 and a gRNA directed against a non-targeting sequence (NT) or HDAC3. Subsequent puromycin selection generated a pooled population of NT or HDAC3 knockout (HDAC3 KO) cells, and immunoblot was used to verify deletion (Figure 2A, S2B-D). HDAC3 KO reduced cell growth rates across all four cell lines (Figure S2E), consistent with the anti-tumor growth phenotype of HDAC3 deletion observed *in vivo*.

To identify the transcriptional programs regulated by HDAC3 in Kras-driven NSCLC cells, we profiled these cell lines by RNA sequencing (RNA-seq). Since HDAC3 KO reduces lung tumor cell growth in KL and KP cells *in vitro* and *in vivo*, we hypothesized that a common mechanism may be engaged upon HDAC3 KO across genotypes, and therefore explored genes commonly deregulated upon HDAC3 KO. Overlap of the RNA-seq datasets across the two KL cell lines and two KP cell lines +/- HDAC3 KO using two different gRNAs identified a stringent set of 38 genes consistently deregulated upon HDAC3 KO in all cell lines profiled (adj. p-value < 0.05, fold > +/-0.5). 26 of these genes were upregulated upon HDAC3 KO (Figure 2B), and 12 were downregulated upon HDAC3 KO (Figure S2F). The "Senescence and Autophagy in Cancer" pathway and the "NFKB1" (NF-kB) transcription factor (TF) were the most enriched terms associated with the genes upregulated upon HDAC3 KO (Figure S2G). p65 RelA/NF-kB is the well-established TF responsible for inducing the expression of the required Senescence Associated Secretory Phenotype (SASP) gene expression program, engaged as a cell undergoes the largely irreversible program of cell cycle arrest known as senescence (11-14). Gene Set Enrichment Analysis (GSEA) confirmed the upregulation of the SASP Senescence and NF-kB target gene sets upon HDAC3 KO in KL and KP cells (Figure 2C, S2H).

We next performed HDAC3 ChIP sequencing (ChIP-seq) in NT and HDAC3 KO cells to identify direct HDAC3 targets in KL LJE1 cells (Figure 2D, S2I). Overlap with the RNA-seq data from KL LJE1 cells revealed that 628 (17%) of the 3,728 HDAC3 peaks were associated with genes differentially expressed upon HDAC3 KO. 364 peaks were associated with 268 genes downregulated upon HDAC3 KO, and 264 peaks were associated with 200 genes upregulated upon HDAC3 KO (Figure 2E). Motif enrichment analysis of HDAC3-bound

genomic regions revealed that the NF-kB/p65 motif was the top *de novo* motif enriched uniquely among genes upregulated upon HDAC3 KO (Figure 2F), suggesting that in NSCLC lung cancer cells HDAC3 directly binds near p65 and represses p65 target gene expression. Notably, we did not observe differences in histone acetylation at the HDAC3-bound genomic regions associated with upregulated gene expression (Figure S2J), suggesting that HDAC3 regulation at these targets is independent of histone acetylation control. Thus, we hypothesized that HDAC3 deletion induces expression of the SASP gene cassette via de-repression of p65.

The SASP genes previously defined to be induced upon engagement of Oncogene-Induced Senescence in a p65-dependent manner (11) exhibit elevated expression levels upon HDAC3 KO in KL cells (Figure 2G). To test if p65 was required for the induction of these genes following HDAC3 deletion, we knocked out p65 in HDAC3 KO cells using CRISPR/Cas9 (Figure 2H). qRT-PCR confirmed that the SASP genes *IL-1a*, *Cxcl5*, and *Ccl20* are induced upon HDAC3 KO in a p65-dependent manner (Figure S2K). RNA-seq on these cells revealed two clusters of genes induced upon HDAC3 KO in a p65-dependent manner (Figure 2I, S2L), confirming that in NSCLC cells HDAC3 represses the p65 gene expression program which includes SASP genes. Mechanistically, HDAC3 has been shown to repress NF-kB activity by directly deacetylating p65 (15-17), although the engagement of this molecular mechanism *in vivo* has not been widely reported. Repression of NF-kB function by HDAC3 has been observed in macrophages (18), but has not been reported in the many other HDAC3-tissue specific knockouts. We have identified that in both KL and KP NSCLC cells, HDAC3 actively represses the NF-kB/p65 transcriptional program, resulting in repression of the tumor cell senescence program. This suggests, importantly, that HDAC3-targeting inhibitors can be employed to modulate p65 activity and the senescence program.

To explore if HDAC3 is repressing p65 and the SASP senescence program *in vivo*, we analyzed histological sections from KL-HDAC3 and KP-HDAC3 mice (Figure 1). Analysis of H&E sections revealed that KL-HDAC3-deleted tumors exhibit unusual epithelial cell morphology characterized by enlarged cytoplasm (Figure 2J). Immunohistochemistry (IHC) for senescence marker p21 and p16 revealed that HDAC3 deleted tumors exhibit elevated levels of both of these markers (Figure 2K), consistent with increased rates of senescence upon HDAC3 deletion *in vivo*. Furthermore, KL-HDAC3 and KP-HDAC3 tumors displayed aberrant recruitment of immune cells to the periphery of and infiltrating the tumor compared to wildtype controls (Figure 2J, S2M). Based on our molecular model, we hypothesized that the HDAC3-dependent immune cell recruitment could be due to de-repression of the SASP program, and sought to determine the identity of the recruited immune cells. IHC identified that CD3+ T-cells are present within KL and KP tumors deleted for HDAC3 to a greater extent than in wildtype tumors of either genotype (Figure 2L, S2N). F4/80+ macrophages, NKp46+ NK cells, and Ly6g+ neutrophils did not exhibit this HDAC3-dependent pattern (Figure S2O). We reasoned that if this T-cell recruitment was due to p65/NF-kB-driven induction of the SASP program, p65 target gene expression should

be elevated in HDAC3 deleted in tumors. Consistently, IHC identified elevated levels of Cxcl5 in HDAC3 KO tumors (Figure 2L, S2N), a key SASP target gene that is among the core genes consistently transcriptionally deregulated in an HDAC3- and p65-dependent manner (Figure 2B, G, I). Thus, HDAC3 is an *in vivo* regulator of the SASP cellular senescence program in lung tumors.

Next, HDAC3 ChIP-seq was performed on KL and KP primary tumors to identify genome wide, endogenously bound HDAC3 target loci *in vivo* (Figure S3A-B, 3A). 1522 peaks were bound by HDAC3 in both KL and KP tumors (Figure 3A), corresponding to 753 non-redundant genes with at least one HDAC3 binding site within +/-25 kilobases of the TSS. We queried the expression pattern of these 753 genes across individual primary tumors isolated from four different Kras-driven lung tumor GEMMs; Kras, KP, KL, and KPL (Figure 3B). A large fraction of these genes exhibited an LKB1-dependent transcriptional pattern, suggesting that an LKB1-dependent mechanism may be mediating differential regulation of a subset of these target genes bound by HDAC3 in both KL and KP tumors. Comparing gene expression between KL versus Kras primary tumors, we found that 39% of the 753 HDAC3 target genes were differentially expressed upon LKB1 loss (Figure S3C). Motif enrichment analysis of the HDAC3-bound sites common to KL and KP tumors (Figure 3A) identified the top enriched *de novo* motif to be that of the transcription factor NKX2-1 (TTF-1) (Figure 3C), a clinical biomarker of lung adenocarcinoma which has an established role enforcing a lineage-specific differentiation program in lung and lung ADC (19, 20). NKX2-1 is an appreciated but undruggable central regulator of LUAD growth and identity. Therefore, identifying druggable regulators of NKX2-1 function is of great interest. While the p65 motif was also identified in this analysis, its enrichment was lower than that of the NKX2-1 motif, suggesting that HDAC3 may interact with p65 at a smaller subset of target genes, whereas HDAC3 interplay with NKX2-1 may occur at a broader set of targets. This analysis suggested an unexpected functional overlap between HDAC3 and NKX2-1, and co-immunoprecipitation experiments confirmed that endogenous NKX2-1 interacts with HDAC3 in KL LJE1 cells (Figure 3D).

To explore if NKX2-1 and HDAC3 co-regulate a set of transcriptional targets, we used CRISPR/Cas9 to delete NKX2-1 in KL LJE1 cells (Figure 3E), and profiled these cells by RNA-seq. Plotting gene expression in KL LJE1 NT or HDAC3 KO cells for the genes most de-regulated upon NKX2-1 KO revealed that 15/18 (83%) are also modulated upon HDAC3 KO (Figure S3D), revealing that the most NKX2-1-dependent genes are nearly all under the control of HDAC3. To query the extent to which HDAC3 is involved in the regulation of NKX2-1 target genes across a broader set of genes, we extended this analysis to the 68 genes deregulated upon NKX2-1 KO by the stronger gRNA (SR), and found that 49/68 (72%) of NKX2-1 target genes were also modulated upon HDAC3 KO in these cells (data not shown) and 21/68 (31%) were associated with HDAC3 ChIP-seq peaks. This suggests that nearly three quarters of the entire NKX2-1 transcriptional program is co-regulated by HDAC3. We found that of the 28

genes deregulated upon NKX2-1 KO and HDAC3 KO, 21/22 (96%) were downregulated and 6/6 (100%) were upregulated upon loss of both NKX2-1 and HDAC3 (Figure S3E). Thus, HDAC3 KO and NKX2-1 KO affect gene expression changes with the same directionality. Consistently, using previously published gene expression data from $Kras^{mut}$ tumors tamoxifen-induced to delete NKX2-1 (19), we found that genes downregulated upon NKX2-1 in $Kras^{mut}$ tumors were negatively enriched upon HDAC3 KO, and genes upregulated upon NKX2-1 loss in $Kras^{mut}$ tumors were positively enriched for upon HDAC3 KO in KL LJE1 cells (Figure S3F).

To assess what fraction of the total HDAC3 transcriptional response is regulated by NKX2-1, we plotted gene expression from NT and NKX2-1 KO cells for all genes differentially expressed upon HDAC3 KO in both KL LJE1 and KL LJE7 cells (Figure S3G, 3F). Of the genes upregulated upon HDAC3 KO, 35/171 (21%) were also upregulated but only 5/171 (3%) downregulated upon NKX2-1 KO. Of the genes downregulated upon HDAC3 KO, 62/165 (38%) were also downregulated and none upregulated upon NKX2-1 KO. 10/40 (25%) of the HDAC3 and NKX2-1 co-regulated genes upregulated upon inactivation of either factor had associated HDAC3 ChIP-seq peaks, whereas 23/62 (37%) of the downregulated co-regulated genes had associated HDAC3 peaks.

One co-regulated target gene of NKX2-1 and HDAC3 (Figure 3F) in KL LJE1 cells is *Fgfr1*. Fgfr1, Fibroblast Growth Factor Receptor 1, is one of four receptor tyrosine kinases that make up the FGFR protein family. FGFRs are receptors for Fibroblast Growth Factors (FGFs), have been widely implicated in promoting tumor growth, and multiple small molecular inhibitors of FGFRs are in various stages of development as cancer therapies (21, 22). We found that *Fgfr1* mRNA was downregulated upon both NKX2-1 KO and HDAC3 KO, and was associated with an HDAC3 ChIP-seq peak. Western blotting identified robust reduction in FGFR1 protein level upon HDAC3 KO or NKX2-1 KO in KL LJE1 cells (Figure 3G), confirming that HDAC3 and NKX2-1 coordinately regulate FGFR1 in KL cells.

To explore FGFR1 regulation in KP cells, we used CRISPR/Cas9 to delete NKX2-1 in KP T3 cells. Surprisingly, we found that neither HDAC3 KO nor NKX2-1 KO altered FGFR1 protein levels in KP T3 cells (Figure S3H), suggesting differential engagement of the HDAC3/NKX2-1 complex in the regulation of this target in KL versus KP cells. To query if this was unique to FGFR1 or if FGFR1 was an indication of broader functional differences between HDAC3/NKX2-1 in KL versus KP cells, we profiled KP T3 cells deleted for HDAC3 or NKX2-1 (Figure S3H) by RNA-seq. Performing analysis on data from KP T3 cells comparable to that done on data from KL LJE1 cells (Figure 3F, S3D, G) revealed that HDAC3 and NKX2-1 coordinately repress the expression of a set of common target genes in KP T3 cells (Figure S3I-J, 3H). This is in contrast to KL LJE1 cells, where HDAC3 and NKX2-1 predominantly promote the expression of their common target genes. 20/24 (83%) of the most stringent NKX2-1-dependent genes were also HDAC3-dependent (Figure S3I), and all were upregulated upon

deletion of NKX2-1 or HDAC3. Considering data from only the stronger NKX2-1 gRNA, 149/202 (74%) of the NKX2-1-dependent genes (all upregulated upon NKX2-1 KO) were HDAC3-dependent, with 136/149 (91%) upregulated and 13/149 (9%) downregulated upon HDAC3 KO (data not shown). Conversely, 388 genes were deregulated upon HDAC3 KO in KP T3 cells; 254 upregulated and 134 downregulated (Figure S3J). 159/254 (63%) were upregulated upon HDAC3 KO or NKX2-1 KO, whereas 68/134 (51%) were downregulated upon HDAC3 KO or NKX2-1 KO (Figure 3H). Considering the distinctly stronger magnitude of change of upregulated genes compared to downregulated genes, this data suggests that HDAC3 and NKX2-1 cooperate to repress a set of common target genes in KP T3 cells. This is in contrast with KL LJE1 cells where HDAC3 and NKX2-1 promote the expression of a set of common target genes. Consistent with HDAC3 and NKX2-1 cooperating to regulate divergent gene programs in KL versus KP cells, little overlap was observed between the co-regulated genes in KL LJE1 and KP T3 cells (Figure S3K). Notably, HDAC3-mediated repression of p65 target gene expression was observed consistently across these same KL and KP lung tumor cell lines regardless of genotype (Figure 2). In contrast to HDAC3 repression of p65, the data regarding NKX2-1 raises the hypothesis that HDAC3 and NKX2-1 may co-regulate different gene programs depending on the tumor genotype.

Since FGFR1 was regulated by HDAC3 and NKX2-1 in a genotype-dependent manner, we utilized it as an example with which to explore the divergence of HDAC3/NKX2-1 co-regulatory function between KL and KP cells. We found that, in primary tumors, *Fgfr1* mRNA is elevated in LKB1 KO compared to LKB1 WT tumors (Figure S4A). Deletion of FGFR1 with CRISPR/Cas9 confirmed that FGFR1 KO reduced KL LJE1 cell growth rates (Figure S4B), supporting a role for FGFR1 in sustaining tumor cell growth. In The Cancer Genome Atlas (TCGA) Lung Adenocarcinoma (LUAD) dataset, high *FGFR1* mRNA correlated with poor patient outcome and, interestingly, 25% of the *FGFR1*-high tumors harbor *STK11* (LKB1) mutation (Figure S4C). Moreover, FGFR1 has been identified to mediate resistance to the FDA-approved MEK inhibitor, Trametinib, that acts downstream of Kras to suppress signaling through the mitogen-activated protein kinase (MAPK) cascade (23). Despite the high rate of Kras mutation in LUAD (~30%), therapeutic targeting of the Kras pathway remains a major challenge in part because therapies directed against Kras effectors activate compensatory or parallel pathways that limit their efficacy as single agents. Current efforts are directed toward elucidating which combination therapy approaches would potentiate clinical benefit from Kras effector inhibitors. Manchado et al. found that co-treatment of Trametinib with the FGFR1 inhibitor Ponatinib induced tumor regression in the KP lung tumor model where Trametinib treatment alone is largely ineffective due to rapidly acquired resistance (23).

Since HDAC3 supports FGFR1 protein expression in KL LJE1 cells (Figure 3G), we hypothesized that HDAC inhibition may be an alternative approach to blocking the induction of FGFR1 by long-term Trametinib treatment in lung cancer cells. We therefore performed short-

term (3 day) and long-term (13 day) treatments with Vehicle or Trametinib. In KL LJE1 cells, FGFR1 protein was strongly induced upon 13 day Trametinib in a manner that could be rescued by co-treatment of Trametinib plus Entinostat, a clinically well-tolerated Class I HDAC inhibitor (Figure 4A). This implies that HDAC inhibitors which target HDAC3 such as Entinostat can block the induction of a transcriptional program that is engaged upon Trametinib resistance. Interestingly, in KP T3 cells, 13 day Trametinib treatment did not induce FGFR1 levels (Figure S4D).

To test if FGFR1 is part of a larger HDAC3-dependent transcriptional cassette that becomes hijacked upon Trametinib resistance in lung cancer cells, we profiled KL LJE1 and KP T3 cells treated as in Figure 4A and S4D by RNA-seq. First, we found that Entinostat treatment induced expression of the same "TNFa Signaling Via NFkB" and "SASP Fridman Senescence" gene sets (Figure 4B, S4E) which enriched upon genetic deletion of HDAC3 (Figure 2C, S2H) in both KL LJE1 and KP T3 cells. Importantly, this confirms that HDAC3 functions as an upstream repressor of the p65/NF-kB and SASP programs in both KL and KP cells in a manner which can be therapeutically targeted using Entinostat, even in the context of Trametinib resistance. However, 13 day Trametinib treatment compared to Vehicle did not enrich for these gene sets, indicating that Trametinib alone does not induce NF-kB repression. Thus, while Entinostat robustly activates NF-kB/SASP in the presence of Trametinib resistance, this mechanism does not appear to be unique to Trametinib resistant cells.

Based on the behavior of FGFR1, we were also interested in looking for NKX2-1 and HDAC3 common targets that become induced upon 13 day Trametinib treatment in a manner rescued by Entinostat. To identify the genes behaving in this pattern, we first defined the genes upregulated upon 13 day Trametinib compared to 13 day Vehicle in KL LJE1 cells, and then plotted the gene expression across all conditions for these 2,141 genes (Figure 4C). The expression of 285/2141 (13%) genes was uniquely induced upon 13 day Trametinib (not upon 3 day Trametinib) in a manner rescued upon co-treatment of Entinostat. One of these 285 genes was *Nkx2-1*itself (Figure 4C, top right), unbiasedly confirming that NKX2-1 induction is a component of long-term Trametinib resistance in KL cells that can be rescued by HDAC inhibition.

To explore if a broader set of NKX2-1-dependent genes are behaving similarly, we queried these 285 Trametinib-induced, Entinostat-rescued genes against RNA-seq data from NKX2-1 KO cells (Figure 4C, bottom right). Indeed, this gene set was negatively enriched upon NKX2-1 KO, with 38/285 (13%) genes downregulated upon NKX2-1 KO in basal conditions. We hypothesized that Entinostat rescues the induction of NKX2-1 target gene expression through inhibition of HDAC3, and thus predicted that a set of HDAC3 direct target genes would also behave in a Trametinib- and Entinostat-dependent manner. Of the 2,933 unique genes associated with at least one HDAC3 ChIP-seq binding site, 112 genes were induced upon 13 day Trametinib treatment in a manner rescued by Entinostat (Figure 4D). We plotted gene expression from

Kras, KP, KL, and KPL primary GEMM lung tumor RNA-seq and found that 43/112 (38%) genes are expressed in an LKB1-dependent manner (Figure S4F). Together, we have identified a set of direct HDAC3 target genes which display LKB1-dependent gene expression in primary tumors, and whose expression is induced in tumor cells as a component of targeted therapy resistance in a manner that can be rescued by HDAC inhibition.

To explore the clinical value of these genes, we queried their expression across a TCGA human Lung Adenocarcinoma dataset (Firehose Legacy). We found that one of the most LKB1-dependent of these 43 HDAC3 target genes, *AVPI1* (Figure 4E-G), was highly expressed (EXP>1.8) in 30/586 (5%) TCGA human tumor samples. These 30 patients had significantly poorer overall survival (30.29 versus 49.8 median months overall) (Figure 4H) and time disease free (data not shown). 11/18 (61.11%) *AVPI1*-high tumors with mutational data harbored *STK11* mutation, the most frequently mutated gene in this group, while only 29/212 (13.68%) of non-*AVPI1*-high tumors had *STK11* mutation. Considering only tumors with Kras amplification or mutation at G12, 8/100 (8%) tumors had high *AVPI1*. These patients had even shorter overall survival (8.48 versus 88.07 median months overall) (Figure S4G) and, of those with mutational data, 5/7 (71.43%) harbored *STK11* mutation and 1/7 had deep deletion of *STK11*. This suggests that our molecular signature datasets can predict patients destined for poor outcome and those who harbor LKB1 mutant tumors.

One implication is that high levels of *AVPI1* mRNA could be a biomarker of aggressive LKB1-mutant lung tumors, and this subgroup of patients – for whom outcome is grim and no targeted therapy options exist - may benefit from Entinostat treatment, perhaps even as a compassionate use indication. Future experiments to define if the Trametinib-resistant, Entinostat-dependent gene signature in KL cells is solely a biomarker or also critical for supporting tumor growth will further clarify the predictive power of these HDAC3 target signatures, and will help elucidate if the combination of Trametinib plus Entinostat is a viable therapeutic approach for leveraging the utility of both of these inhibitors as targeted therapy for LKB1 mutant tumors. This data also motivates exploration of Entinostat treatment in settings where resistance to primary therapy is mediated by repression of senescence, including standard of care chemotherapy treatments. We propose that the potential of HDAC3-selective inhibitors in precision medicine should be seriously considered and further explored.

Acknowledgements
This study was supported by grants to R.J.S. from the NIH (R35CA220538, P01CA120964) and The Leona M. and Harry B. Helmsley Charitable Trust grant #2012-PG- MED002. L.J.E. was supported by a postdoctoral fellowship from the American Cancer Society (PF-15-037-01-DMC). S.N.B was supported by NCI training grant 5T32CA009370 to the Salk Institute Cancer Center and NCI 5F32CA206400. This work was supported by the NGS and the Razavi Newman Integrative Genomics and Bioinformatics Core Facilities of the Salk Institute with funding from the NIH-NCI CCSG: P30 014195, the Chapman Foundation, and the Helmsley Charitable Trust. Tissue Technology Shared Resource is supported by a National Cancer Institute Cancer Center Support Grant (CCSG Grant P30CA23100).

Author Contributions
L.J.E designed all experiments, performed all experiments except as noted here, and wrote the paper. S.D.C., S.N.B, and J.T.B. assisted with cloning and KO cell line generation and validation. D.S.R. assisted with animal husbandry. T.J.R. assisted with genotyping and BLI imaging. L.J.E. and R.J.S. conceived the project, and R.J.S. supervised the project and wrote and edited the paper.

REFERENCES

1. Emmett MJ, Lazar MA. Integrative regulation of physiology by histone deacetylase 3. Nat Rev Mol Cell Biol. 2019;20(2):102-15. Epub 2018/11/06. doi: 10.1038/s41580-018-0076-0. PubMed PMID: 30390028; PMCID: PMC6347506.
2. Emmett MJ, Lim HW, Jager J, Richter HJ, Adlanmerini M, Peed LC, Briggs ER, Steger DJ, Ma T, Sims CA, Baur JA, Pei L, Won KJ, Seale P, Gerhart-Hines Z, Lazar MA. Histone deacetylase 3 prepares brown adipose tissue for acute thermogenic challenge. Nature. 2017;546(7659):544-8. Epub 2017/06/15. doi: 10.1038/nature22819. PubMed PMID: 28614293; PMCID: PMC5826652.
3. Sun Z, Miller RA, Patel RT, Chen J, Dhir R, Wang H, Zhang D, Graham MJ, Unterman TG, Shulman GI, Sztalryd C, Bennett MJ, Ahima RS, Birnbaum MJ, Lazar MA. Hepatic Hdac3 promotes gluconeogenesis by repressing lipid synthesis and sequestration. Nat Med. 2012;18(6):934-42. Epub 2012/05/09. doi: 10.1038/nm.2744. PubMed PMID: 22561686; PMCID: PMC3411870.
4. Sun Z, Feng D, Fang B, Mullican SE, You SH, Lim HW, Everett LJ, Nabel CS, Li Y, Selvakumaran V, Won KJ, Lazar MA. Deacetylase-independent function of HDAC3 in transcription and metabolism requires nuclear receptor corepressor. Mol Cell. 2013;52(6):769-82. Epub 2013/11/26. doi: 10.1016/j.molcel.2013.10.022. PubMed PMID: 24268577; PMCID: PMC3877208.
5. Knutson SK, Chyla BJ, Amann JM, Bhaskara S, Huppert SS, Hiebert SW. Liver-specific deletion of histone deacetylase 3 disrupts metabolic transcriptional networks. EMBO J. 2008;27(7):1017-28. Epub 2008/03/21. doi: 10.1038/emboj.2008.51. PubMed PMID: 18354499; PMCID: PMC2323257.
6. Hollstein PE, Eichner LJ, Brun SN, Kamireddy A, Svensson RU, Vera LI, Ross DS, Rymoff TJ, Hutchins A, Galvez HM, Williams AE, Shokhirev MN, Screaton RA, Berdeaux R, Shaw RJ. The AMPK-Related Kinases SIK1 and SIK3 Mediate Key Tumor-Suppressive Effects of LKB1 in NSCLC. Cancer Discov. 2019;9(11):1606-27. Epub 2019/07/28. doi: 10.1158/2159-8290.CD-18-1261. PubMed PMID: 31350328; PMCID: PMC6825547.
7. Eichner LJ, Brun SN, Herzig S, Young NP, Curtis SD, Shackelford DB, Shokhirev MN, Leblanc M, Vera LI, Hutchins A, Ross DS, Shaw RJ, Svensson RU. Genetic Analysis Reveals AMPK Is Required to Support Tumor Growth in Murine Kras-Dependent Lung Cancer Models. Cell Metab. 2019;29(2):285-302 e7. Epub 2018/11/13. doi: 10.1016/j.cmet.2018.10.005. PubMed PMID: 30415923; PMCID: PMC6365213.
8. Svensson RU, Parker SJ, Eichner LJ, Kolar MJ, Wallace M, Brun SN, Lombardo PS, Van Nostrand JL, Hutchins A, Vera L, Gerken L, Greenwood J, Bhat S, Harriman G, Westlin WF, Harwood HJ, Jr., Saghatelian A, Kapeller R, Metallo CM, Shaw RJ. Inhibition of acetyl-CoA carboxylase suppresses fatty acid synthesis and tumor growth of non-small-cell lung cancer in preclinical models. Nat

Med. 2016;22(10):1108-19. Epub 2016/09/20. doi: 10.1038/nm.4181. PubMed PMID: 27643638; PMCID: PMC5053891.
9. Shackelford DB, Abt E, Gerken L, Vasquez DS, Seki A, Leblanc M, Wei L, Fishbein MC, Czernin J, Mischel PS, Shaw RJ. LKB1 inactivation dictates therapeutic response of non-small cell lung cancer to the metabolism drug phenformin. Cancer Cell. 2013;23(2):143-58. Epub 2013/01/29. doi: 10.1016/j.ccr.2012.12.008. PubMed PMID: 23352126; PMCID: PMC3579627.
10. Liu Y, Marks K, Cowley GS, Carretero J, Liu Q, Nieland TJ, Xu C, Cohoon TJ, Gao P, Zhang Y, Chen Z, Altabef AB, Tchaicha JH, Wang X, Choe S, Driggers EM, Zhang J, Bailey ST, Sharpless NE, Hayes DN, Patel NM, Janne PA, Bardeesy N, Engelman JA, Manning BD, Shaw RJ, Asara JM, Scully R, Kimmelman A, Byers LA, Gibbons DL, Wistuba, II, Heymach JV, Kwiatkowski DJ, Kim WY, Kung AL, Gray NS, Root DE, Cantley LC, Wong KK. Metabolic and functional genomic studies identify deoxythymidylate kinase as a target in LKB1-mutant lung cancer. Cancer Discov. 2013;3(8):870-9. Epub 2013/05/30. doi: 10.1158/2159-8290.CD-13-0015. PubMed PMID: 23715154; PMCID: PMC3753578.
11. Chien Y, Scuoppo C, Wang X, Fang X, Balgley B, Bolden JE, Premsrirut P, Luo W, Chicas A, Lee CS, Kogan SC, Lowe SW. Control of the senescence-associated secretory phenotype by NF-kappaB promotes senescence and enhances chemosensitivity. Genes Dev. 2011;25(20):2125-36. Epub 2011/10/08. doi: 10.1101/gad.17276711. PubMed PMID: 21979375; PMCID: PMC3205583.
12. Campisi J. Cellular Senescence and Lung Function during Aging. Yin and Yang. Ann Am Thorac Soc. 2016;13 Suppl 5:S402-S6. Epub 2016/12/23. doi: 10.1513/AnnalsATS.201609-703AW. PubMed PMID: 28005423; PMCID: PMC5291472.
13. Chan ASL, Narita M. Short-term gain, long-term pain: the senescence life cycle and cancer. Genes Dev. 2019;33(3-4):127-43. Epub 2019/02/03. doi: 10.1101/gad.320937.118. PubMed PMID: 30709901; PMCID: PMC6362810.
14. Kuilman T, Michaloglou C, Mooi WJ, Peeper DS. The essence of senescence. Genes Dev. 2010;24(22):2463-79. Epub 2010/11/17. doi: 10.1101/gad.1971610. PubMed PMID: 21078816; PMCID: PMC2975923.
15. Chen L, Fischle W, Verdin E, Greene WC. Duration of nuclear NF-kappaB action regulated by reversible acetylation. Science. 2001;293(5535):1653-7. Epub 2001/09/05. doi: 10.1126/science.1062374. PubMed PMID: 11533489.
16. Kiernan R, Bres V, Ng RW, Coudart MP, El Messaoudi S, Sardet C, Jin DY, Emiliani S, Benkirane M. Post-activation turn-off of NF-kappa B-dependent transcription is regulated by acetylation of p65. J Biol Chem. 2003;278(4):2758-66. Epub 2002/11/07. doi: 10.1074/jbc.M209572200. PubMed PMID: 12419806.
17. Ziesche E, Kettner-Buhrow D, Weber A, Wittwer T, Jurida L, Soelch J, Muller H, Newel D, Kronich P, Schneider H, Dittrich-Breiholz O, Bhaskara S, Hiebert SW, Hottiger MO, Li H, Burstein E, Schmitz ML, Kracht M. The coactivator role of histone deacetylase 3 in IL-1-signaling involves deacetylation of p65 NF-kappaB. Nucleic Acids Res. 2013;41(1):90-109. Epub 2012/10/23. doi: 10.1093/nar/gks916. PubMed PMID: 23087373; PMCID: PMC3592411.
18. Nguyen HCB, Adlanmerini M, Hauck AK, Lazar MA. Dichotomous engagement of HDAC3 activity governs inflammatory responses. Nature. 2020;584(7820):286-90. Epub 2020/08/08. doi: 10.1038/s41586-020-2576-2. PubMed PMID: 32760002.
19. Snyder EL, Watanabe H, Magendantz M, Hoersch S, Chen TA, Wang DG, Crowley D, Whittaker CA, Meyerson M, Kimura S, Jacks T. Nkx2-1 represses a latent gastric differentiation program in lung adenocarcinoma. Mol Cell. 2013;50(2):185-99. Epub 2013/03/26. doi: 10.1016/j.molcel.2013.02.018. PubMed PMID: 23523371; PMCID: PMC3721642.
20. Yamaguchi T, Hosono Y, Yanagisawa K, Takahashi T. NKX2-1/TTF-1: an enigmatic oncogene that functions as a double-edged sword for cancer cell survival and progression. Cancer Cell. 2013;23(6):718-23. Epub 2013/06/15. doi: 10.1016/j.ccr.2013.04.002. PubMed PMID: 23763999.
21. Dai S, Zhou Z, Chen Z, Xu G, Chen Y. Fibroblast Growth Factor Receptors (FGFRs): Structures and Small Molecule Inhibitors. Cells. 2019;8(6). Epub 2019/06/21. doi: 10.3390/cells8060614. PubMed PMID: 31216761; PMCID: PMC6627960.

22. Babina IS, Turner NC. Advances and challenges in targeting FGFR signalling in cancer. Nat Rev Cancer. 2017;17(5):318-32. Epub 2017/03/18. doi: 10.1038/nrc.2017.8. PubMed PMID: 28303906.
23. Manchado E, Weissmueller S, Morris JPt, Chen CC, Wullenkord R, Lujambio A, de Stanchina E, Poirier JT, Gainor JF, Corcoran RB, Engelman JA, Rudin CM, Rosen N, Lowe SW. A combinatorial strategy for treating KRAS-mutant lung cancer. Nature. 2016;534(7609):647-51. Epub 2016/06/25. doi: 10.1038/nature18600. PubMed PMID: 27338794; PMCID: PMC4939262.
24. Sanchez-Rivera FJ, Papagiannakopoulos T, Romero R, Tammela T, Bauer MR, Bhutkar A, Joshi NS, Subbaraj L, Bronson RT, Xue W, Jacks T. Rapid modelling of cooperating genetic events in cancer through somatic genome editing. Nature. 2014;516(7531):428-31. Epub 2014/10/23. doi: 10.1038/nature13906. PubMed PMID: 25337879; PMCID: PMC4292871.
25. DuPage M, Dooley AL, Jacks T. Conditional mouse lung cancer models using adenoviral or lentiviral delivery of Cre recombinase. Nat Protoc. 2009;4(7):1064-72. Epub 2009/06/30. doi: 10.1038/nprot.2009.95. PubMed PMID: 19561589; PMCID: PMC2757265.
26. Dobin A, Davis CA, Schlesinger F, Drenkow J, Zaleski C, Jha S, Batut P, Chaisson M, Gingeras TR. STAR: ultrafast universal RNA-seq aligner. Bioinformatics. 2013;29(1):15-21. Epub 2012/10/30. doi: 10.1093/bioinformatics/bts635. PubMed PMID: 23104886; PMCID: PMC3530905.
27. Heinz S, Benner C, Spann N, Bertolino E, Lin YC, Laslo P, Cheng JX, Murre C, Singh H, Glass CK. Simple combinations of lineage-determining transcription factors prime cis-regulatory elements required for macrophage and B cell identities. Mol Cell. 2010;38(4):576-89. Epub 2010/06/02. doi: 10.1016/j.molcel.2010.05.004. PubMed PMID: 20513432; PMCID: PMC2898526.
28. de Hoon MJ, Imoto S, Nolan J, Miyano S. Open source clustering software. Bioinformatics. 2004;20(9):1453-4. Epub 2004/02/12. doi: 10.1093/bioinformatics/bth078. PubMed PMID: 14871861.
29. Saldanha AJ. Java Treeview--extensible visualization of microarray data. Bioinformatics. 2004;20(17):3246-8. Epub 2004/06/08. doi: 10.1093/bioinformatics/bth349. PubMed PMID: 15180930.
30. Hulsen T, de Vlieg J, Alkema W. BioVenn - a web application for the comparison and visualization of biological lists using area-proportional Venn diagrams. BMC Genomics. 2008;9:488. Epub 2008/10/18. doi: 10.1186/1471-2164-9-488. PubMed PMID: 18925949; PMCID: PMC2584113.
31. Cerami E, Gao J, Dogrusoz U, Gross BE, Sumer SO, Aksoy BA, Jacobsen A, Byrne CJ, Heuer ML, Larsson E, Antipin Y, Reva B, Goldberg AP, Sander C, Schultz N. The cBio cancer genomics portal: an open platform for exploring multidimensional cancer genomics data. Cancer Discov. 2012;2(5):401-4. Epub 2012/05/17. doi: 10.1158/2159-8290.CD-12-0095. PubMed PMID: 22588877; PMCID: PMC3956037.
32. Gao J, Aksoy BA, Dogrusoz U, Dresdner G, Gross B, Sumer SO, Sun Y, Jacobsen A, Sinha R, Larsson E, Cerami E, Sander C, Schultz N. Integrative analysis of complex cancer genomics and clinical profiles using the cBioPortal. Sci Signal. 2013;6(269):pl1. Epub 2013/04/04. doi: 10.1126/scisignal.2004088. PubMed PMID: 23550210; PMCID: PMC4160307.

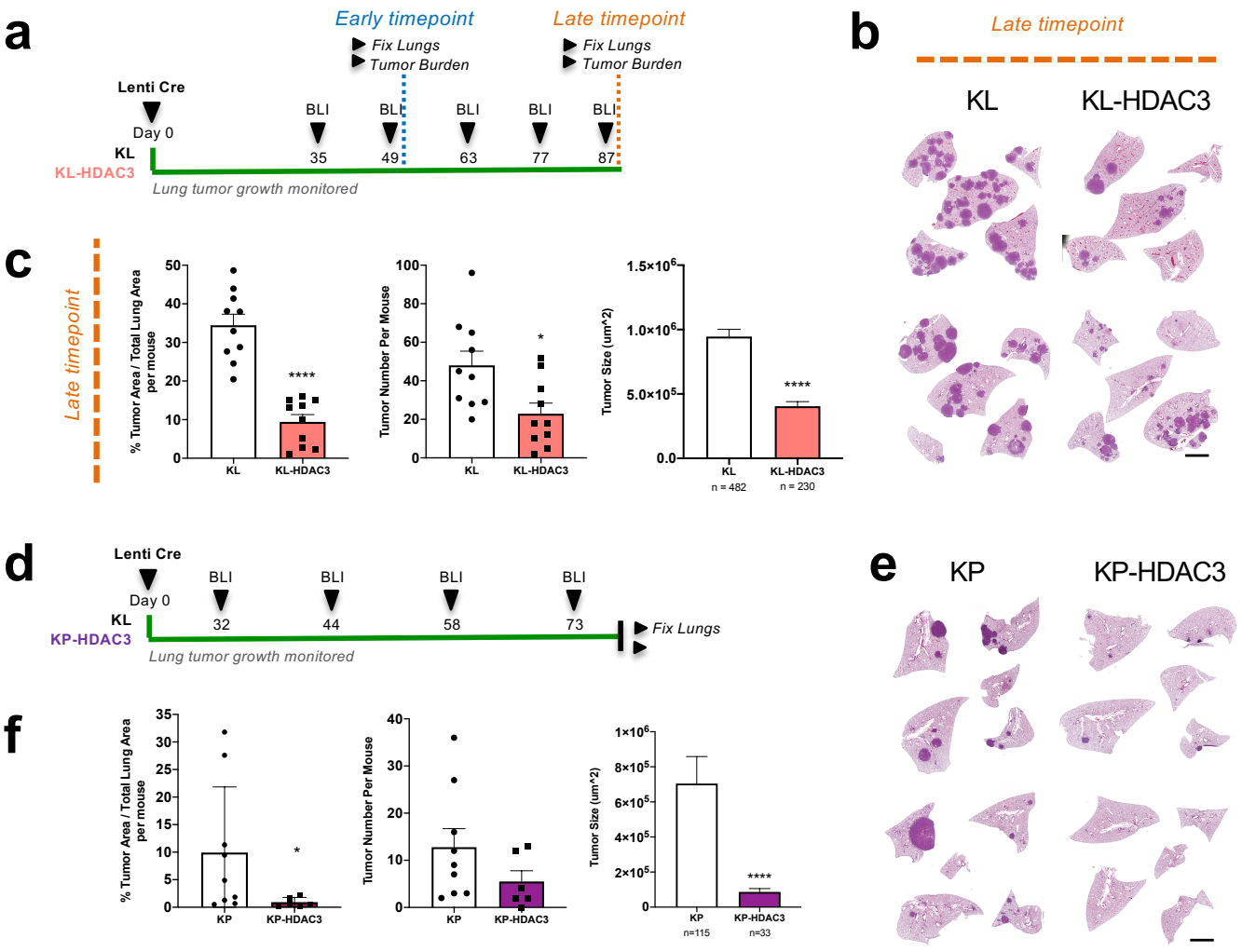

Figure 1. HDAC3 is essential for lung tumorigenesis *in vivo* in KL and KP GEMM models of NSCLC

(A) Schematic of experimental design in $Kras^{G12D/+}$, $LKB1^{L/L}$ (KL) and $KL\text{-}HDAC3^{L/L}$ (KL-HDAC3) mouse models administered Lenti-Cre.

(B) Representative H&E-stained sections from the late timepoint. Scale bar 1000um.

(C) Quantitation from H&E-stained sections from the late timepoint cohort: Tumor area as a percentage of total lung area per mouse, tumor number per mouse, and average tumor size.

(D) Schematic of experimental design in $Kras^{G12D/+}$, $p53^{L/L}$ (KP) and $KP\text{-}HDAC3^{L/L}$ (KP-HDAC3) mouse models administered Lenti-Cre.

(E) Representative H&E-stained sections. Scale bar 1000um.

(F) Quantitation from H&E-stained sections: Tumor area as a percentage of total lung area per mouse, tumor number per mouse, and average tumor size.

Figure 1

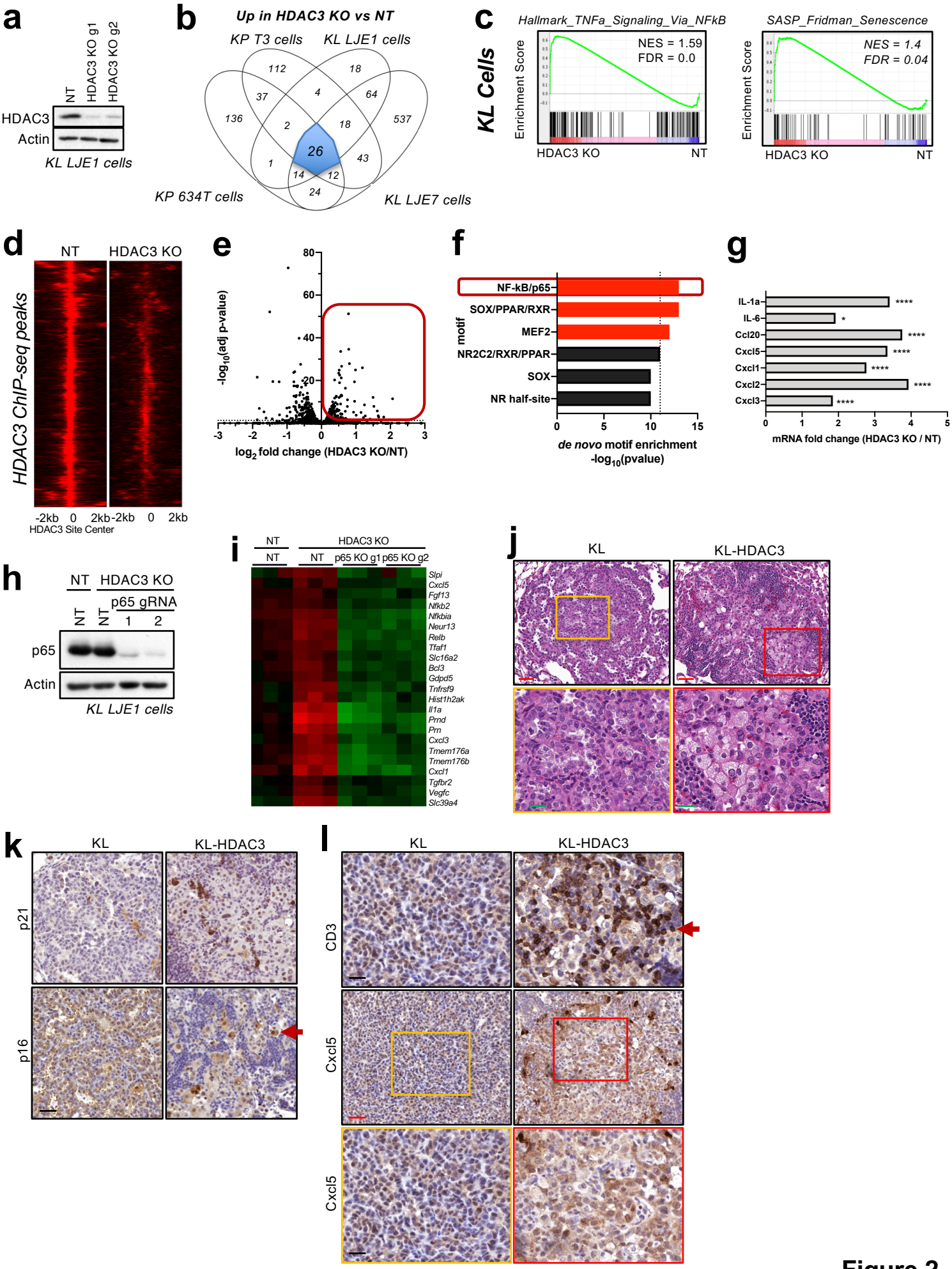
a
NT
HDAC3 KO g1
HDAC3 KO g2
HDAC3
Actin
KL LJE1 cells
b
Up in HDAC3 KO vs NT
KP T3 cells
KL LJE1 cells
KP 634T cells
KL LJE7 cells
112
18
37
4
64
136
2
18
537
26
1
43
14
12
24
c
KL Cells
Hallmark_TNFa_Signaling_Via_NFkB
NES = 1.59
FDR = 0.0
SASP_Fridman_Senescence
NES = 1.4
FDR = 0.04
Enrichment Score
HDAC3 KO
NT
d
NT
HDAC3 KO
HDAC3 ChIP-seq peaks
-2kb 0 2kb
HDAC3 Site Center
e
-log10(adj p-value)
log2 fold change (HDAC3 KO/NT)
f
motif
NF-kB/p65
SOX/PPAR/RXR
MEF2
NR2C2/RXR/PPAR
SOX
NR half-site
de novo motif enrichment
-log10(pvalue)
g
IL-1a
IL-6
Ccl20
Cxcl5
Cxcl1
Cxcl2
Cxcl3
mRNA fold change (HDAC3 KO / NT)
h
NT
HDAC3 KO
p65 gRNA
p65
Actin
KL LJE1 cells
i
HDAC3 KO
NT
p65 KO g1
p65 KO g2
Slpi
Cxcl5
Fgf13
Nfkb2
Nfkbia
Neur13
Relb
Tfaf1
Slc16a2
Bcl3
Gdpd5
Tnfrsf9
Hist1h2ak
Il1a
Prnd
Prn
Cxcl3
Tmem176a
Tmem176b
Cxcl1
Tgfbr2
Vegfc
Slc39a4
j
KL
KL-HDAC3
k
KL
KL-HDAC3
p21
p16
l
KL
KL-HDAC3
CD3
Cxcl5
Cxcl5

Figure 2

Figure 2. HDAC3 represses the NF-kB/p65 SASP transcriptional program in KL and KP NSCLC cells

(A) Western blot analysis of HDAC3 deletion (KO) by CRISPR/Cas9 using two different gRNAs (g1, g2) in polyclonal lysates in KL LJE1 cells.

(B) Overlap of genes upregulated upon HDAC3 KO (using all gRNAs tested) compared to non-targeting (NT) control using RNA-seq data from two KL cells lines (LJE1, LJE7) and two KP cell lines (T3, 634T), with adj. p-value <0.05 and fold change >+/-0.5 cut-offs.

(C) Gene Set Enrichment Analysis (GSEA) plots of the "Hallmark TNFa Signaling Via NFkB" and "SASP Fridman Senescence" gene sets queried against RNA-seq data comparing HDAC3 KO vs NT conditions across KL LJE1 and KL LJE7 cells combined.

(D) 3,728 HDAC3 ChIP-seq peaks identified in KL LJE1 NT cells normalized to NT Input and using HDAC3 ChIP-seq in HDAC3 KO cells as background.

(E) Plot of RNA-seq data from KL LJE1 cells (HDAC3 KO vs NT) for the 468 genes associated with at least one HDAC3 ChIP-seq peak identified in Figure 2D.

(F) Homer *de novo* motif enrichment analysis of the genomic regions bound by HDAC3 in ChIP-seq for the genes upregulated upon HDAC3 KO (red box) in Figure 2E. Motifs enriched uniquely among upregulated genes are shown. Red bars indicates statistically significant motifs.

(G) Plot of gene expression change (RNA-seq data) upon HDAC3 KO vs NT in KL LJE7 cells for p65-dependent SASP genes.

(H) Western blot analysis of p65 deletion in HDAC3 KO cells by CRISPR/Cas9 using two different gRNAs in polyclonal lysates in KL LJE1 cells.

(I) Heatmap of one gene cluster upregulated upon HDAC3 KO in a p65-dependent manner from RNA-seq data generated from cells in Figure 2H.

(J) Representative histopathology images of KL and KL-HDAC3 tumors. Red scale bar 100um, Green scale bar 20um.

(K) Representative images of p21 and p16 IHC in KL and KL-HDAC3 tumors. Scale bar 30um.

(L) Representative images of CD3 and Cxcl5 IHC in KL and KL-HDAC3 tumors. Black scale bar 20um, red scale bar 40um.

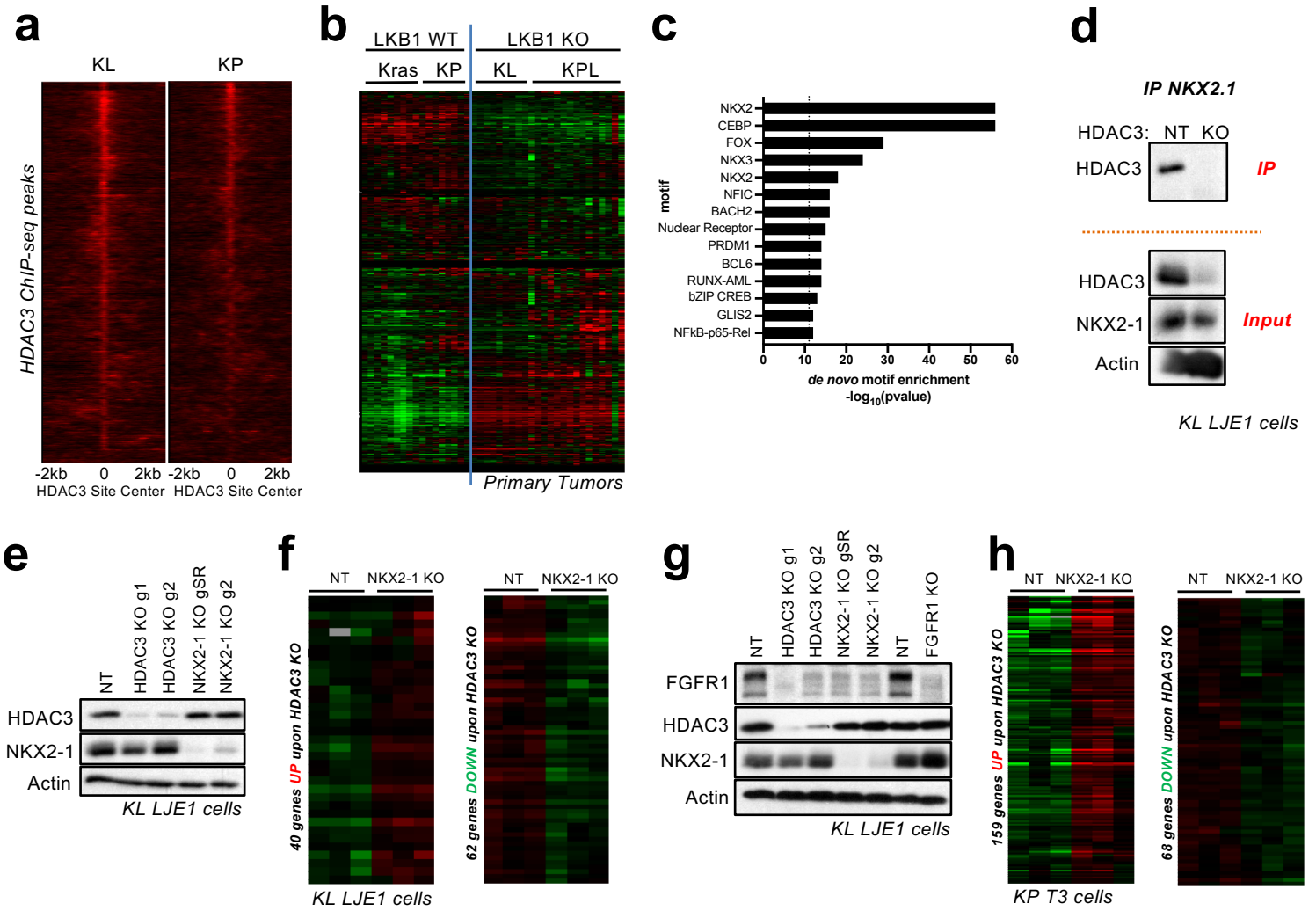

Figure 3. HDAC3 cooperates with NKX2-1

(A) 1522 HDAC3 ChIP-seq peaks common to KL and KP primary tumors.

(B) Heatmap of RNA-seq data from primary tumors from LKB1 WT (Kras, KP) and LKB1 KO (KL, KPL) models for the 753 non-redundant genes associated with at least one HDAC3 ChIP-seq peak within 25kb of the TSS.

(C) Homer *de novo* motif enrichment analysis of the HDAC3-bound peaks in Figure 3A. All significantly enriched motifs are listed.

(D) Western blot analysis of NKX2-1 co-immunoprecipitation with HDAC3 in NT vs HDAC3 KO KL LJE1 cells.

(E) Western blot analysis of HDAC3 and NKX2-1 deletion (KO) by CRISPR/Cas9 using two different gRNAs (gSR, g2 for NKX2-1) in polyclonal lysates in KL LJE1 cells.

(F) Genes commonly upregulated (left) or downregulated (right) upon both HDAC3 KO and NKX2-1 KO in KL cells, as defined from red box regions on heatmap in Figure S4G.

(G) Western blot analysis of FGFR1, HDAC3 and NKX2-1 in NT, HDAC3 KO, NKX2-1 KO, and FGFR1 KO cell lysates from KL LJE1 cells.

(H) Genes commonly upregulated (left) or downregulated (right) upon both HDAC3 KO and NKX2-1 KO in KP T3 cells, as defined from red box regions on heatmap in Figure S4J.

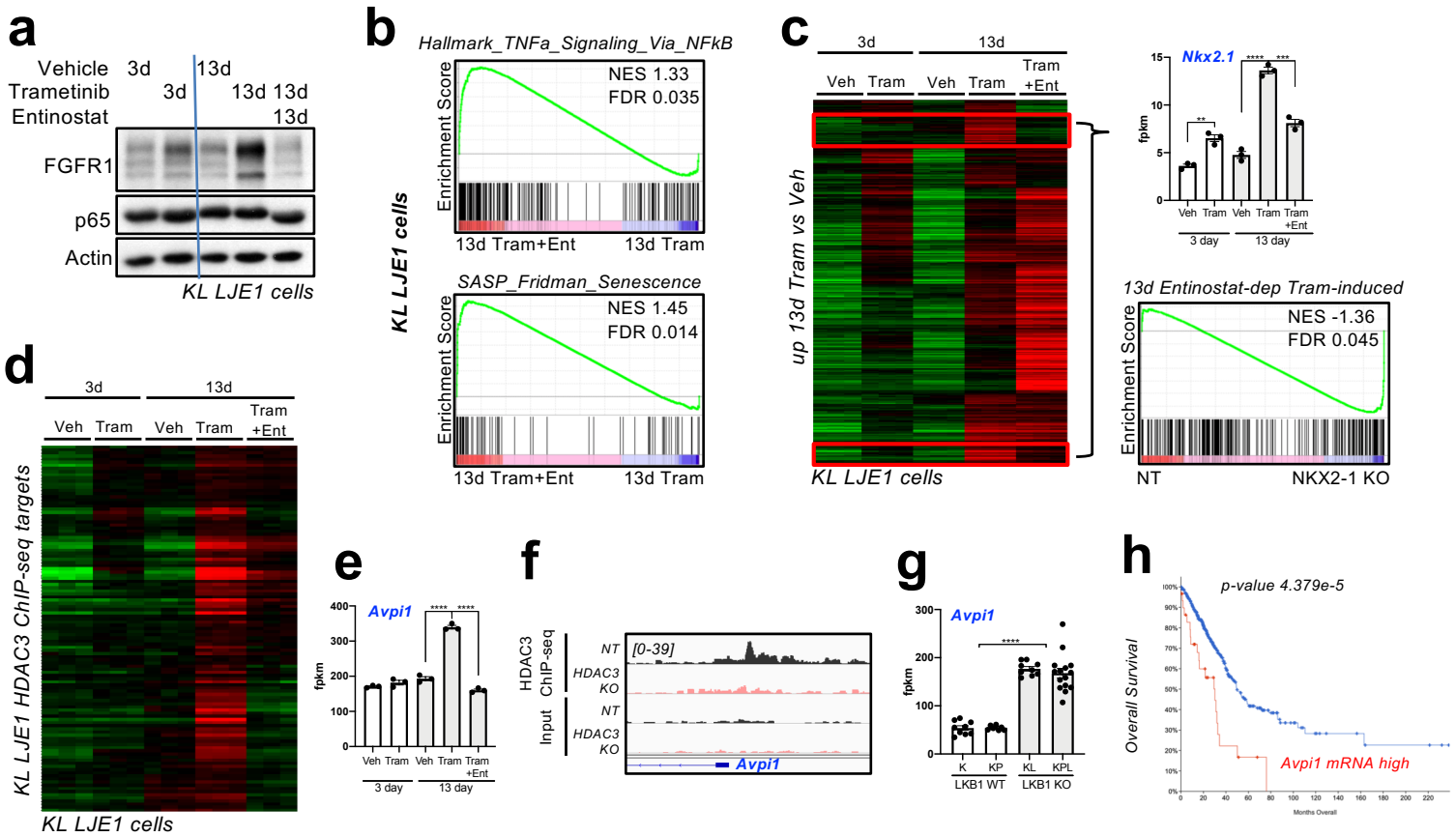

Figure 4. HDAC3 and NKX2-1 regulate the expression of a common set of target genes which is aberrantly engaged upon Trametinib resistance
(A) Western blot analysis of FGFR1 and p65 in protein lysates from KL LJE1 cells treated with Veh, 10nM Trametinib, or 1uM Entinostat for 3 or 13 days.
(B) GSEA plots of the "Hallmark TNFa Signaling Via NFkB" and "SASP Fridman Senescence" gene sets queried against RNA-seq data comparing 13 day Trametinib+Entinostat to 13 day Trametinib conditions in KL LJE1 cells.
(C) *Left:* Heatmap of RNA-seq data across all treatment conditions for the 2,141 genes significantly upregulated (adj. p-value < 0.05, fold > +/-0.5) upon 13 day Trametinib compared to 13 day Vehicle in KL LJE1 cells. Veh, Vehicle; Tram, Trametinib; Ent, Entinostat.
Right, top: Nkx2-1 mRNA levels across all treatment conditions.
Right, bottom: GSEA analysis of the 285 Trametinib-induced, Entinostat-rescued genes queried across RNA-seq data from NKX2-1 KO vs NT KL LJE1 cells.
(D) Heatmap of RNA-seq data across all treatment conditions for the 112 HDAC3 ChIP-seq target genes induced upon Trametinib in a manner rescued by Entinostat.
(E) *Avpi1* mRNA levels across all treatment conditions.
(F) HDAC3 ChIP-seq data in NT and HDAC3 KO KL LJE1 cells at the *Avpi1* genomic locus.
(G) *Avpi1* mRNA expression across Kras (K), KP, KL, and KPL primary tumor RNA-seq data.
(H) Overall survival data for all patients from the Firehose Legacy LUAD TCGA dataset separated between *Avpi1* mRNA high versus low tumors.

Figure 4

MATERIALS AND METHODS

Cell culture and cell lines. All cell lines were incubated at 37 °C and were maintained in an atmosphere containing 5% CO_2. 634T cell were a kind gift from Kwok Wong. KP T3 cells were published in Hollstein et al. *Cancer Discovery*, 2019. Cells were tested for Mycoplasma (Lonza) using manufacturer's conditions and were deemed negative. Cells were grown in Dulbecco's modified Eagles medium (DMEM) plus 10% fetal bovine serum (Gibco) and were continuously maintained under antibiotic selection for stable cell lines. Proliferation assays were performed by plating 2x10^3 cells per well of a 6-well plate, and cells were counted 5 days post-plating. Trametinib was used at 10nM, Entinostat was used at 1uM (long-term treatments) or 2uM (6h treatments), RGFP966 was used at 10uM, and TSA was used at 0.5uM. Treatments were 6h, 3d, or 13d. For long-term treatments, media was changed and fresh drug added every 2 days.

Generating primary tumor cell lines. To generate KL LJE1 and KL LJE7 cell lines, individual primary tumors were dissected from the lungs of KL mice, mechanically dissociated, then digested for 45min in digestion media (10% FBS, pen/strep, 1mg/mLCollagenase/Dispase (Roche) in DMEM) at 37 °C. Cells were strained through 70uM nylon cell strainer, spun at 2000rpm 5min, resuspended in 1mL complete media plus 5uL Fungizone (Lifetech) and plated in a 24 well dish. 24h later, cells were infected by adding 1mL T-antigen-expressing lentivirus to each well. 24h later, viral media was removed and replaced with complete media with Fungizone. Cells were cultured in Fungizone for 4 weeks, then Epcam+ sorted.

CRISPR/Cas9 studies.
Small Guide RNAs (sgRNAs) targeting mouse HDAC3 were selected using the optimized CRISPR design tool (http://crispr.mit.edu). The gSR gRNA sequence targeting NKX2-1 was obtained from Sanchez-Rivera et al. *Nature* 2014 (24), and the other gRNA targeting NKX2-1, g2, was designed with the GPP sgRNA designer (https://portals.broadinstitute.org/gpp/public/analysis-tools/sgrna-design). gRNAs targeting FGFR1 and p65 were designed with the Benchling program (https://www.benchling.com/crispr/). Guides with high targeting scores and low probability of off-target effects were chosen. At least three independent sgRNA sequences were tested for each gene. Oligonucleotides for sgRNAs were synthesized by IDT, annealed in vitro and subcloned into BsmbI-digested lentiCRISPRv.2-puro (Addgene 52961) or lentiCRISPRv.2-hygro (Addgene 98291). Validation of guide specificity was assessed by Western blot of low-passage cells. Oligonucleotide sequences are listed in Supplemental Table S1.

Lentiviral production and Titering
Lentiviruses made from pLentiCRISPRv.2 were produced by co-transfection of the lentiviral backbone constructs and packaging plasmids pSPAX2 (Addgene 12260) and pMD2.G (Addgene 12259). Lipofectamine 2000 (Thermo Fisher Scientific) was used as a transfection reagent at a ratio of 3:1 lipofectamine/DNA. Viral supernatant was collected from 293 cells 48 post-transfection, 0.45um-filtered, supplemented with polybrene, and applied to destination cells for 24h. Destination cells were allowed to recover from infection 24h before being subjected to selection with 2ug/ml puromycin or 150ug/mL hygromycin. Resulting stably transduced lines were frozen down immediately after selection.
Large-scale viral preps of Lenti Pgk-Cre (a gift from Tyler Jacks) were made by the University of Iowa Viral Vector Core. Titering: Lentiviral preps for mouse experiments (PGK-Cre) were functionally titered by transduction of a reporter line (293-LSL-GFP), which turns on expression of GFP upon Cre-mediated recombination and allows quantitation of functional titers derived from the percent of GFP-positive cells.

Mouse Studies

All procedures using animals were approved by the Salk Institute Institutional Animal Care and Use Committee (IACUC). All mice were maintained on the FVB/n background. **Kras** (*Kras*$^{LSLG12D/+;}$ *R26*$^{LSL;luc/luc}$); **KL** (*Kras*$^{LSLG12D/+;}$ *Lkb1*$^{fl/fl}$;*R26*$^{LSL;luc/luc}$), **KP** (*Kras*$^{LSLG12D/+;}$ *p53*$^{fl/fl}$;*R26*$^{LSL;luc/luc}$), and **KPL** (*Kras*$^{LSLG12D/+;}$ *Lkb1*$^{fl/fl}$;*p53*$^{fl/fl}$;*R26*$^{LSL;luc/luc}$) mice in FVB/n have been previously described(9) (7). The *Hdac3*$^{fl/fl}$ conditional floxed mouse has also been described (5). In this study, *Hdac3*$^{fl/fl}$ was crossed into the FVB/n K background before crossing into the KL or KP genotypes to generate KL-HDAC3$^{fl/fl}$ and KP-HDAC3$^{fl/fl}$ experimental mice. All experiments used a mixture of female and male mice. Experimental endpoint was defined across experiments as the time point at which the experimental cohorts of KL or KP mice reached tumor burden of 10^8 mean photon flux, or earlier as indicated. At endpoint, all mice in that experiment were collected at that point. All animals at experimental endpoint were included for analysis of lung tumor burden and tumor size analysis. No animals were excluded from longitudinal BLI measurements and graphs. Lentivirus (4x10^5 pfu/mouse) was delivered by intratracheal intubation to each mouse, according by the protocol of DuPage (25).

BLI imaging

Bioluminescent imaging was performed biweekly using an IVIS Spectrum (Caliper Life Sciences). Mice were injected intraperitoneally with 150mg/kg D-luciferin (Caliper Life Science, Hopkinton MA), anesthetized with isoflurane and imaged both ventrally and dorsally 10 minutes post luciferin injection. The total lung photon flux for each animal is calculated by the combination of ventral and dorsal photon flux calculated within a region of interest (ROI) encompassing the thorax.

Immunohistochemistry and image analysis

Lungs from mice were collected at each experimental endpoint as noted in the Figures, and were fixed in formalin for 18-22hrs, transferred to 70% ethanol and paraffin-embedded (FFPE) at the Tissue Technology Shared Resources at UCSD. 5µm sections from FFPE tissues were prepared and stained with hematoxylin and eosin. For immunohistochemistry, slides were deparaffinized and rehydrated, and antigen retrieval was performed for 13min at high heat (~95°C) in citrate buffer. Endogenous peroxidase activity was quenched with 10min hydrogen peroxide in methanol. Using the ImmPress HRP Ig (Peroxidase) Polymer Detection Kits (Vector Labs), slides were blocked, incubated overnight with primary antibody diluted in blocking buffer, and secondary antibody steps were carried out according to the manufacturer's instructions. Staining was visualized with ImmPACT DAB peroxidase substrate (Vector Labs, SK-4105), and further counterstained with hematoxylin, dehydrated through ethanol and xylenes, and mounted with Cytoseal 60 (Thermo Scientific). H&E- and immunostained slides were scanned using a Perkin Elmer Slide Scanner (Panoramic MIDI Digital Side Scanner) for further downstream analysis using the Panoramic Viewer software and Inform v2.1 image analysis software (Cambridge Research and Instrumentation).

Lung tumor burden

Total lung tumor burden was quantitated from H&E sections using Inform v2.1 image analysis software (Cambridge Research and Instrumentation) in a non-biased manner. In brief, the Trainable Tissue Segmentation method was trained to identify tumor, normal lung, vessel and space. This program was then applied to all H&E images, and each of the resulting mapped images was then screened to verify that accurate tissue segmentation had occurred. The quantitation data from this analysis was then used to calculate the percentage of tumor area as normalized to total lung area (tumor area + normal lung area).

Tumor Size Quantitation
Quantitation of each individual tumor was measured from H&E sections using morphometric analysis in Panoramic viewer software (Perkin Elmer), which calculates the size of each identified tumor by area in squared microns. The area of all tumors found in the 5 lobes of each mouse was exported and compiled to plot the number of tumors per mouse, and the average size of every tumor in the cohort.

mRNA preparation and qRT-PCR.
mRNA was collected from cells harvested within 2 passages post-thaw. mRNA was prepared using the Quick-RNA Miniprep kit (Zymo Research), including DNase treatment. cDNA was synthesized from 2 µg of RNA using SuperScript III (Life Technologies), and qPCR was carried out with diluted cDNA, appropriate primers, and SYBR Green PCR master mix (ThermoFisher Scientific) using a C1000 Thermal Cycler (BioRad). Relative mRNA levels were calculated using the 2− Ct method, using *Tbp* as an internal control.

mRNA-sequencing
RNA was isolated using the Quick-RNA MiniPrep kit (Zymo Research), including a DNase treatment. RNA integrity (RIN) numbers were determined using the Agilent TapeStation prior to library preparation. mRNA-seq libraries were prepared using the TruSeq RNA library preparation kit (version 2), according to the manufacturer's instructions (Illumina). Libraries were quantified, pooled, and sequenced by single-end 50 base pairs using the Illumina HiSeq 2500 platform at the Salk Next-Generation Sequencing Core. Raw sequencing data were demultiplexed and converted into FASTQ files using CASAVA (version 1.8.2).

Bioinformatic analysis of RNA-seq data
Sequenced reads were quality-tested using the online FASTQC tool (http://www.bioinformatics.babraham.ac.uk/projects/fastqc) and aligned to the mouse mm10 genome using the STAR aligner version 2.4.0k (26). Raw gene expression was quantified across all annotated exons using HOMER (27), and differential gene expression was carried out using the getDiffExpression.pl command. Differentially expressed genes were defined as having a false discovery rate (FDR) <0.05 and a log2 fold change >0.5.
GSEA was carried out with the GenePattern interface (https://genepattern.broadinstitute.org) using preranked lists generated from FDR values. Queried datasets used were (1) GSEA Gene Set "Hallmark_TNFA_Signaling_Via NFKB" M5890, (2) SASP Fridman Senescence, and (3) gene lists from genes differentially expressed upon Tamoxifen-driven NKX2-1 KO in Kras tumors (19). Heatmaps were generated by clustering using the Cluster 3.0 program (log2 transform data, center genes, Hierarchical clustering with average linkage) (28), and then visualized with Java TreeView version 1.1.6r4 (29).

ChIP-sequencing
<u>*Primary tumors.*</u> Individually dissected, flash frozen primary tumors were combined from 3 different mice into one pool of 130mg of primary tumors per replicate per genotype. Equivalent masses of tumors were used from each of the three mice to ensure equal representation. Two independent pools of tumors per genotype were processed separately to generate two biological replicate pool of crosslinked, sonicated chromatin for ChIP. 4 independent ChIPs were performed on each pool of sonicated chromatin, and then pooled together to generate one replicate for ChIP-sequencing. To crosslink, tumors were dounce homogenized in crosslinking buffer (1% Formladehyde in PBS) and incubated with end-over-end rotation for 15min at room temperature, and then quenched with 2.5M glycine 5min. Samples were spun at 600g for 5min, washed with cold PBS, and resuspended in ChIP buffer (RIPA) (see "Immunoprecipitation" for recipe) with protease inhibitors. Samples were sonicated in a Covaris LE 220 for 8min (Duty Factor 2, 105 Watts, 200 cycles/burst), spun down, and the

supernatant saved. For each ChIP, 100uL lysate was combined with 900uL ChIP buffer, while 50uL was used for Input. 10ug of Hdac3 ab7030 antibody and 2ug H3K27ac ab4729 antibody was used for each ChIP. Lysate was incubated overnight with antibody. 20uL washed and pre-blocked Protein A Dynabeads were incubated 2hrs rotating with each sample at 4degC. Washes were performed with 5min incubations of each buffer while rotating at 4degC. Samples were washed 3X with cold ChIP buffer, 1X with room temperature ChIP buffer, and 1X with room temperature TE pH 8, and then spun down. Elution of ChIP and Input samples was done by incubating samples with Elution buffer (50mM Tris/Hcl pH 7.5, 10mM EDTA, 1% SDS) overnight at 65degC. Beads were pelleted and discarded, and 200uL of eluate was combined with 194uL low-EDTA TE and 100ug proteinase K, and incubated 2hrs at 37degC. 8uL RNase A was added and samples incubated 30min at 37degC. Minelute PCR purification kit (Qiagen 28006) was used to isolate DNA, which was eluted in 15uL EB at 55degC. 4 ChIPs were combined into one sample for ChIP-sequencing.

KL LJE1 cells. ChIP-seq was carried out on DSG+Formaldehyde crosslinked, sonicated nuclear extracts. Cells were washed in PBS and then crosslinked by 30min incubation in 2mM DSG (Di(N-succinimidyl) glutarate, Thermo Fisher NC0054325). Aspirate, and incubate 15min with 1% formaldehyde, before 5min of quench with 125mM glycine. Cells were washed in cold PBS, scraped, and spun down, and washed again in PBS before nuclei isolation. Nuclei were isolated by resuspension in CiA NP-Rinse 1 (50mM HEPES, 140mM NaCl, 1mM EDTA, 10% glycerol, 0.5% NP-40, 0.25% Triton X100), incubated 10min at 4degC with end-over-end rotation, then centrifuged at 1,200g for 5min at 4degC. Samples were then resuspended in CiA NP-Rinse 2 (10mM Tris pH 8.0, 1mM EDTA, 0.5mM EGTA, 200mM NaCl), incubated 10min at 4degC with end-over-end rotation, and centrifuged at 1,200g for 5min at 4degC. Tubes were washed 2X with Covaris Shearing Buffer (0.1% SDS, 1mM EDTA pH 8, 10mM Tris HCl pH 8) to remove salt, centrifuged at 1,200g at 4degC 3min. Samples were diluted to a concentration of $2.5x10^6$ cells/130uL in ChIP buffer (RIPA) (50mM Tris-HCl pH 7.5, 140mM NaCl, 1mM EDTA, 1% Triton X-100, 0.1% NaDOC (sodium deoxycholate), 0.1% SDS) with protease inhibitors, and sonicated in a Covaris LE 220 for 8min (Duty Factor 2, 105 Watts, 200 cycles/burst). Sonicated material was spun down and supernatant was used for ChIP. Lysate from 5 million cells was diluted in ChIP buffer to 1mL final volume. 50uL was used for Input. 10ug of Hdac3 CST-85057 antibody and 2ug H3K27ac ab4729 antibody was used for each ChIP. Lysate was incubated overnight with antibody. 20uL washed and pre-blocked Protein A Dynabeads were incubated 2hrs rotating with each sample at 4degC. Washes were performed with 5min incubations of each buffer while rotating at 4degC. Samples were washed 3X with cold ChIP buffer, 1X with room temperature ChIP buffer, and 1X with room temperature TE pH 8, and then spun down. Elution of ChIP and Input samples was done by incubating samples with Elution buffer (50mM Tris/Hcl pH 7.5, 10mM EDTA, 1% SDS) overnight at 65degC. Beads were pelleted and discarded, and 200uL of eluate was combined with 194uL low-EDTA TE and 100ug proteinase K, and incubated 2hrs at 37degC. 8uL RNase A was added and samples incubated 30min at 37degC. Minelute PCR purification kit (Qiagen 28006) was used to isolate DNA, which was eluted in 15uL EB at 55degC.

Bioinformatic analysis of ChIP-seq data

Sequenced reads were aligned to the mouse mm10 genome using the STAR aligner version 2.4.0k (26). HOMER (27) was used for data processing. For KL LJE1 cell line ChIP-seq data, peaks were called using the getDifferentialPeaksReplicates.pl command using HDAC3 ChIP-seq data from NT cells as target (-t), HDAC3 ChIP-seq data from HDAC3 KO cells as background (-b), and Input sequencing data from NT cells as input (-i), with -style factor and -F 3. For primary tumor ChIP-seq data, peaks were called for each replicate individually using the findPeaks command with parameters -style factor -F 3, using HDAC3 ChIP-seq as target and Input sequencing data as Input (-i). Peaks were merged using the mergePeaks command to generate a

consolidated file containing all HDAC3 ChIP-seq peaks identified in KL and KP tumors. The getDifferentialPeaks command with -F 3 -same was used to identify peaks bound in both KL and KP tumors. The annotatePeaks.pl command with the -ghist -hist 25 option was used to visualize binding at each peak independently across samples, and Java TreeView was used to visualize the output. The annotatePeaks.pl command with -hist 25 was used to plot average reads across all peaks relative to peak center for each replicate separately. BED files were also generated and visualized with Integrative Genomics Viewer (IGV) version 2.5.1.

Homer motif enrichment analysis

Homer motif enrichment analysis: http://homer.ucsd.edu/homer/motif/.

Web-based analysis tools

Pathway analysis was performed with Enrichr: http://amp.pharm.mssm.edu/Enrichr. 4-way Venn diagrams were plotted using Venny 2.1 (Oliveros, J.C. (2007-2015) Venny. An interactive tool for comparing lists with Venn's diagrams, (https://bioinfogp.cnb.csic.es/tools/venny/). Area-proportional Venn diagrams were plotted using BioVenn (30) (https://biovenn.nl).

Western blots

Protein lysates in CST buffer (20mM Tris pH 7.5, 150mM NaCl, 1% Triton X-100, 50mM NaF, 1mM EDTA, 1mM EGTA, 2.5mM PyroPhosphate, 2mM beta-glycerol-phophate, 1mM orthovanadate, 0.01mM Calyculan A) with protease inhibitors were equilibrated for protein levels using a BCA protein assay kit (Pierce), resolved on 8% SDS-PAGE gels, and transferred to membrane. Membranes were blocked in milk, incubated overnight at 4degC in diluted primary antibody, washed with TBS-T, incubated 1hr in secondary antibody diluted in in TBS-T plus milk, washed in TBS-T, and developed using SuperSignal ECL. Secondary antibodies used were anti-rabbit (Millipore AP132P) and anti-mouse (Millipore AP124P). Nuclear fractions were isolated using a NE-PER nuclear and cytoplasmic extraction kit (Thermofisher) under manufacturers conditions.

Immunoprecipitation

Immunoprecipitation was carried out on DSP-crosslinked, sonicated nuclear lysates. Cells were washed in PBS and then crosslinked by 30min incubation in 1mM DSP (dithiobis(succinimidyl propionate), Thermo Scientific 22585), followed by 5min of quench with 2.5M glycine. Cells were washed in PBS, scraped, and spun down, and washed again in PBS before nuclei isolation. Nuclei were isolated by resuspension in CiA NP-Rinse 1 (50mM HEPES, 140mM NaCl, 1mM EDTA, 10% glycerol, 0.5% NP-40, 0.25% Triton X100), incubated 10min at 4degC with end-over-end rotation, then centrifuged at 1,200g for 5min at 4degC. Samples were then resuspended in CiA NP-Rinse 2 (10mM Tris pH 8.0, 1mM EDTA, 0.5mM EGTA, 200mM NaCl), incubated 10min at 4degC with end-over-end rotation, and centrifuged at 1,200g for 5min at 4degC. Tubes were washed twice with Covaris Shearing Buffer (0.1% SDS, 1mM EDTA pH 8, 10mM Tris HCl pH 8) to remove salt, centrifuged at 1,200g at 4degC 3min. Samples were diluted to a concentration of $2.5x10^6$ cells/130uL in ChIP buffer (RIPA) (50mM Tris-HCl pH 7.5, 140mM NaCl, 1mM EDTA, 1% Triton X-100, 0.1% NaDOC (sodium deoxycholate), 0.1% SDS) with protease inhibitors, and sonicated in a Covaris LE 220 for 8min (Duty Factor 2, 105 Watts, 200 cycles/burst). Sonicated material was spun down and supernatant was used for IP: 400uL material was incubated with 3uL NKX2-1 antibody (Abcam ab76013) per IP overnight with rotation at 4degC. 20uL prewashed Protein A Dynabeads were added per tube, and incubated 4hrs at 4deg with rotation. Samples were washed 5x with CST buffer (see western blot section) before adding 25uL 6x loading dye and 50uL CST per tube, and eluting by boiling for 5min. Input and IP samples were subsequently assessed by western blot.

TCGA analysis of Firehose LUAD dataset
The results shown are in whole based upon data generated by the TCGA Research Network: http://cancergenome.nih.gov/. TCGA datasets were queried using cBioPortal (www.cbioportal.org) (31) (32). Methods for data generation, normalization and bioinformatics analyses were previously described in the TCGA LUAD publication (Cancer Genome Atlas Research 2014). mRNA data used for this analysis was RNA Seq V2 RSEM with *z*-score thresholds of 1.8.

Antibodies and reagents.
Western blotting. Antibodies from Cell Signaling Technologies (Denvers, MA USA) were diluted 1:1,000: Hdac3 CST-85057, p65 CST-6956, Fgfr1 CST-9740. Nkx2-1 was from Abcam ab76013 and was diluted 1:1,500 From Sigma-Aldrich, anti-actin (#A5441) was diluted 1:10,000.
Immunohistochemistry. Abcam antibodies ab5690 was used at 1:150 to detect CD3, ab198505 was used at 1:100 to detect Cxcl5/6, and ab211542 was used at 1:150 to detect p16. Cell Signaling Technologies CST-70076 was used at 1:250 to detect F4/80. R&D Systems AF2225 was used at 5ug/mL to detect NKp46/NCR1. BioXcell BE0075-1 was used at 1:1,000 to detect Ly6g. SantaCruz sc-6246 was used at 1:50 to detect p21.
ChIP. Hdac3 from Abcam ab7030 was used on primary tumors, and Hdac3 from Cell Signaling Technologies CST-85057 was used on KL LJE1 cells.
IP. Nkx2-1 raised in rabbit from (Abcam ab76013) was used to immunoprecipitate, and HDAC3 raised in mouse (CST-3949) was used to detect co-immunoprecipitated HDAC3.

Statistical analyses.
Statistical analyses are described in each figure were all performed using Graph Pad Prism 8.

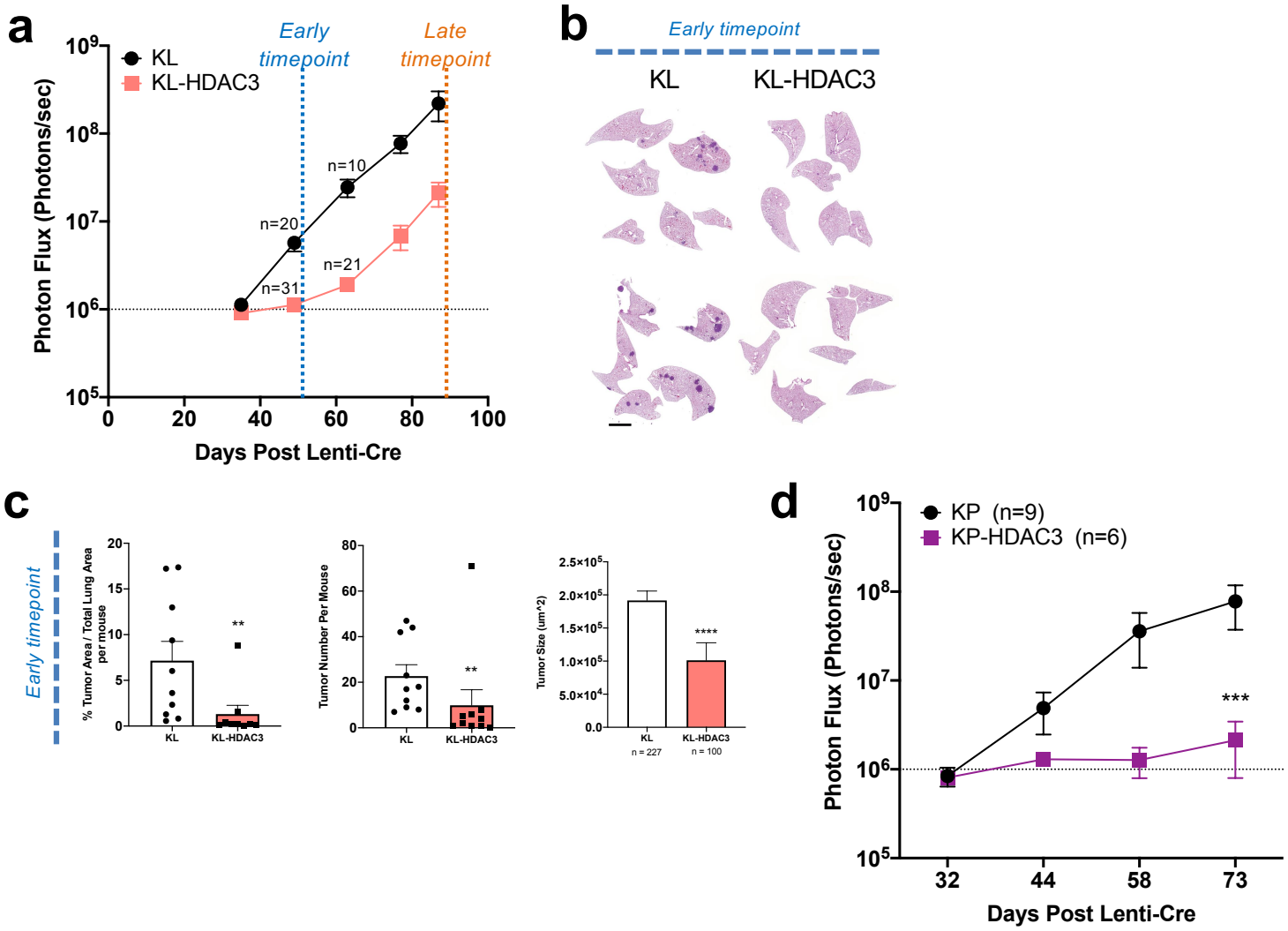

Figure S1.
(A) Average longitudinal BLI data from the KL-HDAC3 experiment.
(B) Representative H&E-stained sections from the KL-HDAC3 early timepoint. Scale bar 1000um.
(C) Quantitation from H&E-stained sections from the early timepoint cohort: Tumor area as a percentage of total lung area per mouse, tumor number per mouse, and average tumor size.
(D) Average longitudinal BLI data from the KP-HDAC3 experiment.

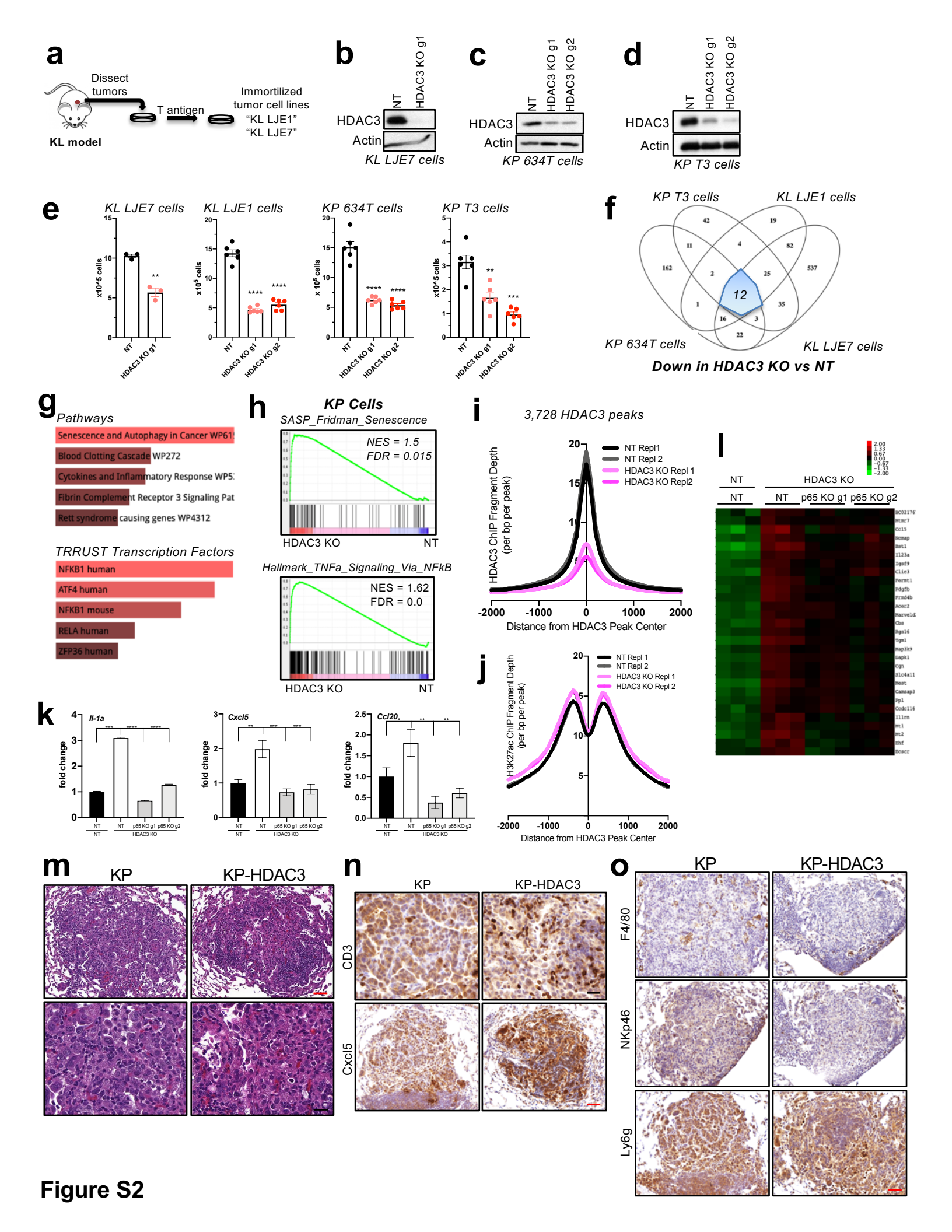
a
Dissect tumors
T antigen
Immortilized tumor cell lines
"KL LJE1"
"KL LJE7"
KL model
b
NT
HDAC3 KO g1
HDAC3
Actin
KL LJE7 cells
c
NT
HDAC3 KO g1
HDAC3 KO g2
HDAC3
Actin
KP 634T cells
d
NT
HDAC3 KO g1
HDAC3 KO g2
HDAC3
Actin
KP T3 cells
e
KL LJE7 cells
KL LJE1 cells
KP 634T cells
KP T3 cells
x10^5 cells
NT
HDAC3 KO g1
HDAC3 KO g2
f
KP T3 cells
KL LJE1 cells
KP 634T cells
KL LJE7 cells
42
19
11
4
82
162
2
25
537
12
1
35
16
3
22
Down in HDAC3 KO vs NT
g
Pathways
Senescence and Autophagy in Cancer WP61
Blood Clotting Cascade WP272
Cytokines and Inflammatory Response WP5
Fibrin Complement Receptor 3 Signaling Pat
Rett syndrome causing genes WP4312
TRRUST Transcription Factors
NFKB1 human
ATF4 human
NFKB1 mouse
RELA human
ZFP36 human
h
KP Cells
SASP_Fridman_Senescence
NES = 1.5
FDR = 0.015
HDAC3 KO
NT
Hallmark_TNFa_Signaling_Via_NFkB
NES = 1.62
FDR = 0.0
HDAC3 KO
NT
i
3,728 HDAC3 peaks
NT Repl1
NT Repl 2
HDAC3 KO Repl 1
HDAC3 KO Repl2
HDAC3 ChIP Fragment Depth (per bp per peak)
Distance from HDAC3 Peak Center
j
NT Repl 1
NT Repl 2
HDAC3 KO Repl 1
HDAC3 KO Repl 2
H3K27ac ChIP Fragment Depth (per bp per peak)
Distance from HDAC3 Peak Center
l
NT
HDAC3 KO
NT
NT
p65 KO g1
p65 KO g2
k
Il-1a
Cxcl5
Ccl20
fold change
NT
p65 KO g1
p65 KO g2
HDAC3 KO
m
KP
KP-HDAC3
n
KP
KP-HDAC3
CD3
Cxcl5
o
KP
KP-HDAC3
F4/80
NKp46
Ly6g

Figure S2

Figure S2.

(A) Schematic of experimental design to establish KL LJE1 and KL LJE7 cell lines from KL primary tumors.

(B) Western blot analysis of HDAC3 KO by CRISPR/Cas9 in polyclonal lysates in KL LJE7 cells.

(C) Western blot analysis of HDAC3 KO by CRISPR/Cas9 in polyclonal lysates in 634T cells.

(D) Western blot analysis of HDAC3 KO by CRISPR/Cas9 in polyclonal lysates in KP T3 cells.

(E) Proliferation assessment 5 days after plating HDAC3 KO or NT cells from KL LJE1, KL LJE7, KP 634T, and KP T3 cell lines.

(F) Overlap of genes downregulated upon HDAC3 KO (using all gRNAs tested) compared to NT using RNA-seq data from KL LJE1, KL LJE7, KP T3, and KP 634T cell lines, with adj. p-value <0.05 and fold change >+/-0.5 cut-offs.

(G) Enrichr Pathway and Transcription analysis of the 26 commonly upregulated genes identified in Figure 2B.

(H) GSEA plots of the “Hallmark TNFa Signaling Via NFkB” and “SASP Fridman Senescence” gene sets queried against RNA-seq data comparing HDAC3 KO vs NT conditions across KP cells.

(I) Average HDAC3 ChIP-seq fragment depth +/-2kb of each peak center for the 3,728 HDAC3 ChIP-seq peaks identified in KL LJE1 NT cells in Figure 2D. Data from each ChIP replicate (Repl) from NT and HDAC3 KO cells is plotted.

(J) Average H3K27ac ChIP-seq fragment depth +/-2kb of each peak center for the HDAC3 ChIP-seq peaks associated with upregulated gene expression upon HDAC3 KO (red box, Figure 2E) in KL LJE1 NT cells. Data from each ChIP replicate (Repl) from NT and HDAC3 KO cells is plotted.

(K) qRT-PCR for *Il-1a*, *Cxcl5*, and *Ccl20* expression in KL LJE1 cells deleted for HDAC3 +/- p65 KO.

(L) Heatmap of the second gene cluster upregulated upon HDAC3 KO in a p65-dependent manner from RNA-seq data generated from cells in Figure 2H.

(M) Representative histopathology images of KP and KP-HDAC3 tumors. Red scale bar 50um, black scale bar 20um.

(N) Representative images of CD3 and Cxcl5 IHC in KP and KP-HDAC3 tumors. Black scale bar 20um, Red scale bar 50um.

(O) Representative images of F4/80, NKp46, and Ly6g IHC in KP and KP-HDAC3 tumors. Scale bar 50um.

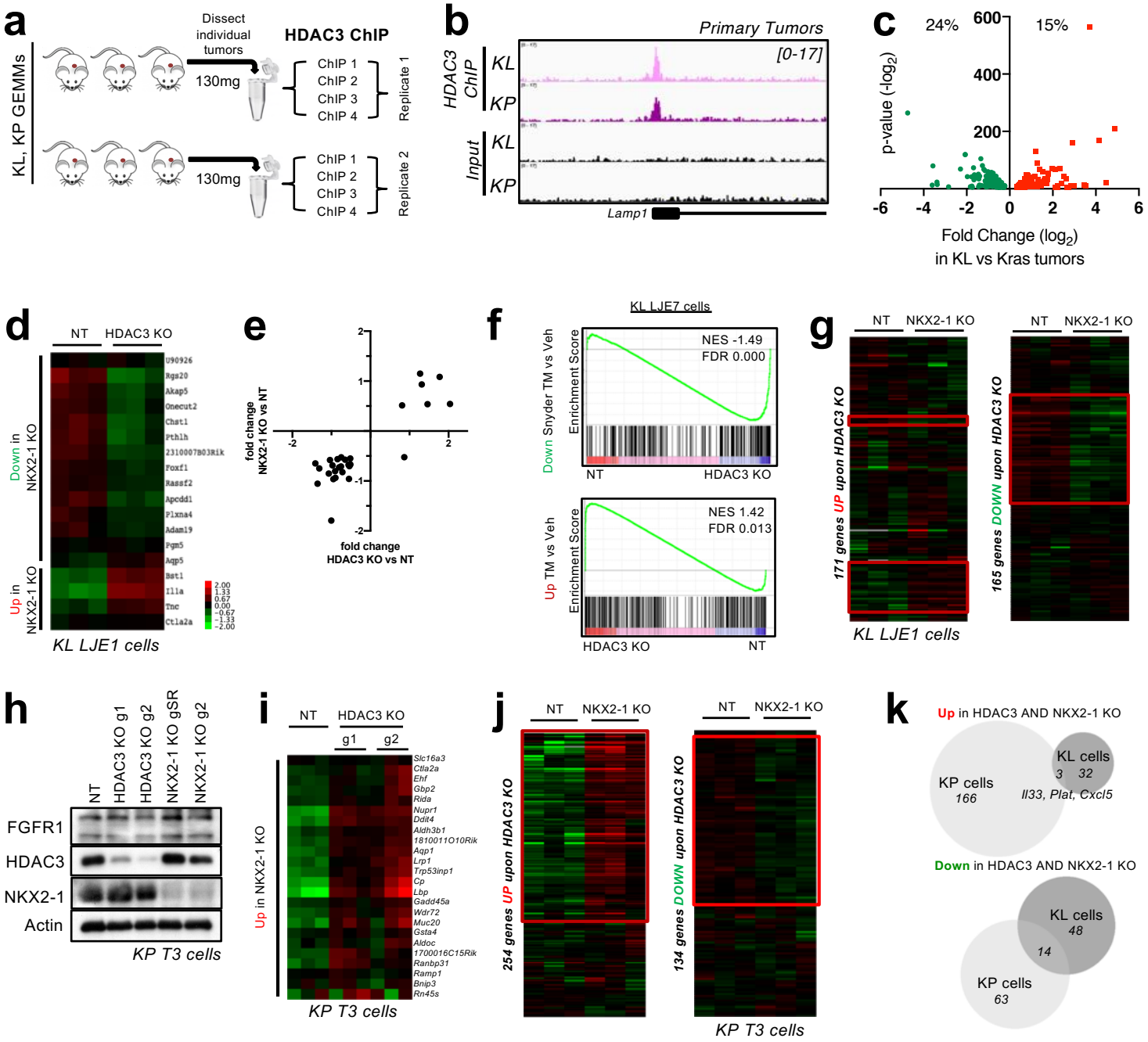

Figure S3.

(A) Schematic of HDAC3 ChIP-seq experimental design in primary KL and KP tumors.

(B) Example of an HDAC3 ChIP-seq peak at a genomic region bound by HDAC3 in both KL and KP primary tumors.

(C) Plot of RNA-seq differential expression between KL versus Kras primary tumors for the HDAC3 target genes in Figure 3A.

(D) Heatmap of RNA-seq data from NT or HDAC3 KO cells for the genes significantly deregulated upon NKX2-1 KO (adj. p-value <0.05, fold +/-0.5) in KL LJE1 cells.

(E) Plot of fold change upon HDAC3 KO compared to NKX2-1 KO for the genes in Figure S4D.

(F) GSEA plots for genes deregulated (downregulated, top plot; or upregulated, bottom plot) upon tamoxifen (TM)-mediated *in vivo* deletion of NKX2-1 in Kras tumors (Snyder et al. Mol Cell, 2013) queried across HDAC3 KO RNA-seq data from KL LJE7 cells.

(G) Heatmap of RNA-seq data from NT or NKX2-1 KO KL LJE1 cells for the genes significantly deregulated upon HDAC3 KO (adj. p-value <0.05, fold +/-0.5) in KL LJE1 and KL LJE7 cells.

(H) Western blot analysis of FGFR1, HDAC3 and NKX2-1 in NT, HDAC3 KO and NKX2-1 KO cell lysates from KP T3 cells.

(I) Heatmap of RNA-seq data from NT or HDAC3 KO cells for the genes significantly deregulated upon NKX2-1 KO (adj. p-value <0.05, fold +/-0.5) in KP T3 cells.

(J) Heatmap of RNA-seq data from NT or NKX2-1 KO KL LJE1 cells for the genes significantly deregulated upon HDAC3 KO (adj. p-value <0.05, fold +/-0.5) in KP T3 cells.

(K) Overlap of genes significantly upregulated (top) or downregulated (bottom) upon both HDAC3 KO and NKX2-1 KO in KP versus KL cells.

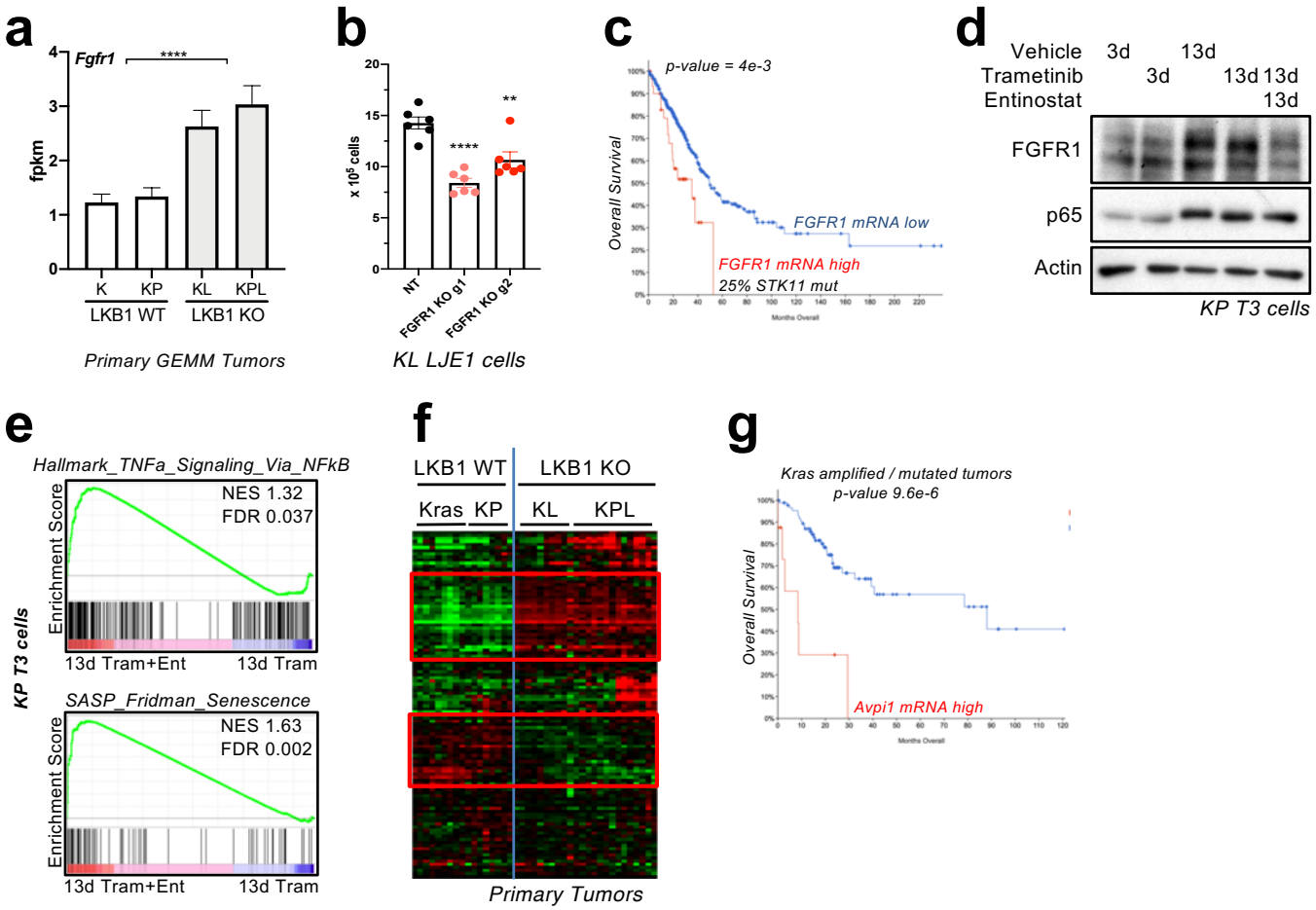

Figure S4.

(A) *Fgfr1* mRNA expression across Kras (K), KP, KL, and KPL primary tumor RNA-seq data.

(B) Proliferation assessment 5 days after plating NT or FGFR1 KO KL LJE1 cells.

(C) Overall survival data from all patients in the Firehose Legacy LUAD TCGA dataset separated between *Fgfr1* mRNA high versus low tumors.

(D) Western blot analysis of FGFR1 and p65 in protein lysates from KP T3 cells treated with Vehicle, 10nM Trametinib, or 1uM Entinostat for 3 or 13 days.

(E) GSEA plots of the “Hallmark TNFa Signaling Via NFkB” and “SASP Fridman Senescence” gene sets queried against RNA-seq data comparing 13 day Trametinib+Entinostat to 13 day Trametinib conditions in KP T3 cells.

(F) Heatmap of RNA-seq data from Kras, KP, KL, and KPL primary tumors for the 112 HDAC3 ChIP-seq target genes induced upon Trametinib in a manner rescued by Entinostat (Figure 4D).

(G) Overall survival data from patients with Kras amplified or mutant tumors in the Firehose Legacy LUAD TCGA dataset separated between *Avpi1* mRNA high versus low tumors.